

SN 2017ati: A luminous type I Ib explosion from a massive progenitor

Z.-H. Peng (彭泽辉)¹, S. Benetti², Y.-Z. Cai (蔡永志)^{3,4,2*}, A. Pastorello², J.-W. Zhao^{5,6**}, A. Reguitti^{2,7}, Z.-Y. Wang^{8,9}, E. Cappellaro², N. Elias-Rosa^{2,10}, Q.-L. Fang¹¹, M. Fraser¹², T. Kangas^{13,14}, E. Kankare¹⁴, Z. Kostrzewska-Rutkowska¹⁵, P. Lundqvist¹⁶, S. Mattila^{14,17}, T. M. Reynolds^{14,18,19}, M. D. Stritzinger²⁰, A. Somero¹⁴, L. Tomasella², S.-P. Pei²¹, Y.-J. Yang²², J.-J. Zhang^{3,4}, and Y. Pan (潘宇)^{1***}

(Affiliations can be found after the references)

Received ; accepted

ABSTRACT

We present optical photometric and spectroscopic observations of the Type I Ib supernova (SN) 2017ati. It reached the maximum light at about 27 d after the explosion and the light curve shows a broad, luminous peak with an absolute r -band magnitude of $M_r = -18.48 \pm 0.16$ mag. At about 50 d after maximum light, SN 2017ati exhibits a decline rate close to that expected from the $^{56}\text{Co} \rightarrow ^{56}\text{Fe}$ radioactive decay, at 0.98 mag per 100 days, as usually observed in SNe I Ib. However, it remains systematically brighter at late times by about 1–2 mag, exceeding the usual upper luminosity range of this class. As a result, modelling the light curve of SN 2017ati with a standard ^{56}Ni decay scenario requires a large nickel mass of up to $\sim 0.37 M_\odot$ and still fails to reproduce the early-time light curve adequately. In contrast, incorporating additional energy input from a magnetar yields a significantly improved fit to the light curve of SN 2017ati, which would reduce the nickel mass to $\sim 0.21 M_\odot$, still close to the upper end of the range typically inferred for SNe I Ib. Comparing the fitted results of SN 2017ati with the known sample of SNe I Ib indicates that its luminosity evolution is best explained by a combination of neutron star spin-down energy and radioactive nickel deposition. From late-time nebular spectra of SN 2017ati, the luminosity of the $[\text{O I}] \lambda\lambda 6300, 6364$ doublet implies an oxygen mass of $\sim 1.82 - 3.34 M_\odot$, and the combination of a $[\text{Ca II}]/[\text{O I}]$ flux ratio of ~ 0.5 with nebular spectral model comparisons favours a progenitor zero-age main-sequence mass of $\geq 17 M_\odot$.

Key words. stars: mass-loss – supernovae: general – supernovae: individual: SN 2017ati

1. Introduction

Core-collapse supernovae (CCSNe) constitute a broad and heterogeneous class of stellar explosions, exhibiting a wide range of observational behaviours that reflect the diversity of progenitor systems and explosion mechanisms. Within this family, Type II SNe are defined by the presence of hydrogen features in photospheric spectra. SNe Ib are distinguished by the absence of hydrogen signatures while displaying strong helium lines, whereas Type Ic events show neither hydrogen nor helium features. SNe I Ib occupy a transitional regime, in which hydrogen features are visible at early epochs but gradually fade as helium lines strengthen, leading to spectral characteristics that increasingly resemble those of SNe Ib at later phases (Filippenko 1997; Gal-Yam 2017; Modjaz et al. 2019).

In addition to the classical spectroscopic categories, several additional sub-classes of CCSNe have been firmly established over the past two decades, including Types Ibn and Icn. Collectively, SNe Ib, Ic, I Ib, Ibn, and Icn are commonly grouped under the class of stripped-envelope SNe (SE-SNe, Clocchiatti et al. 1996; Matheson et al. 2001; Gangopadhyay & Pessi 2025), reflecting progenitor stars that experienced partial or near-complete removal of hydrogen and/or helium layers prior to explosion. Within this population, the majority of SNe I Ib display peak absolute magnitudes fainter than -18.0 mag. However, a small fraction of SNe I Ib are markedly more luminous (e.g. SN 2018gk, DES14X2fna; Bose et al. 2021; Grayling et al.

2021; Gomez et al. 2022). These overluminous events occupy an intermediate luminosity regime between normal CCSNe and superluminous SNe ($M_{\text{peak}} \lesssim -21$ mag; Gal-Yam 2019).

In the standard framework of SNe I Ib, the optical light curve is predominantly powered by the radioactive decay of ^{56}Ni produced during the explosion into ^{56}Co , followed by its subsequent decay to stable ^{56}Fe . Analytical and semi-analytical formulations of this radioactive-decay scenario, such as the Arnett model (Arnett 1982) and the more recent treatment by Khatami & Kasen (2019), enable estimates of key explosion parameters from the observed light curves (Taddia et al. 2018; Stritzinger et al. 2018b; Bersten et al. 2018). By contrast, several other classes of CCSNe are dominated by alternative energy sources, for example strong interaction between the ejecta and circumstellar material in SNe I In (Chevalier 1982; Chugai 1991; Moriya et al. 2013). Even in such cases, a ^{56}Ni -based framework can still provide useful constraints on explosion properties (e.g. Prentice et al. 2016; Meza & Anderson 2020). For events whose luminosity evolution is primarily governed by radioactive decay, including SNe I Ib, a higher peak brightness generally implies a larger synthesized mass of ^{56}Ni required to power the light-curve maximum.

More recently, magnetar-based scenarios have been shown to successfully reproduce the observed light curves of SNe Ic-BL. Within this framework, the luminosity evolution is sustained by a combination of radioactive energy input and additional power supplied by a central engine, arising from the spin-down of a rapidly rotating neutron star (Kasen & Bildsten 2010; Woosley 2010). In particular, Wang et al. (2017) (but see Dessart et al. 2017) showed that a magnetar model can successfully reproduce

* Corresponding authors: caiyongzhi@ynao.ac.cn (CYZ)

** meow.jiewei.zhao@gmail.com (ZJW)

*** panyu@cqupt.edu.cn (PY)

the light curves of the SNe Ic-BL SN 1998bw and SN 2002ap, with magnetar energy dominating within the first ~ 50 d and again at very late phases, thereby explaining the deviations from a pure ^{56}Ni -powered evolution. By contrast, for a subset of X-ray transients linked to SNe Ic-BL, such as EP 250108a/SN 2025kg, one could expect that the early emission post explosion originates from magnetar energy deposition, and not solely from shock-cooling (Eyles-Ferris et al. 2025; Rastinejad et al. 2025; Srinivasaragavan et al. 2025; Zhu et al. 2025; Li et al. 2025b). In these events, multi-wavelength observations show clear evidence for circumstellar interaction, indicating that both magnetar input and ejecta-CSM interaction contribute to the luminosity evolution. These studies provide a direct demonstration that hybrid energy sources may operate in the earliest phases of some broad-line Type Ic SNe, complementing the classical magnetar-powered light curve framework.

In addition, a subset of SNe IIb, such as SNe 1993J (Richmond et al. 1994), 2011fu (Morales-Garoffolo et al. 2015), and 2016gkg (Arcavi et al. 2017; Bersten et al. 2018), display an early-time excess in their light curves prior to the main maximum. This feature is commonly interpreted as emission from post-shock-breakout cooling associated with a progenitor consisting of a compact core embedded within an extended, low-mass envelope (Bersten et al. 2012; Nakar & Piro 2014). The duration of this phase is typically limited to a few days and is not universally detected among SNe IIb, as described in the case of SN 2008ax (Pastorello et al. 2008; Tsvetkov et al. 2009; Taubenberger et al. 2011). When observed, this early bump provides valuable constraints on progenitor properties such as the stellar radius and the role of binary interaction through comparison with hydrodynamic models (Sapir & Waxman 2017).

In this work, we present optical photometric and spectroscopic observations of SN 2017ati, a comparatively luminous member ($M_r = -18.48 \pm 0.16$ mag) of the SN IIb population. This study is structured as follows: Section 2 introduces SN 2017ati. Section 3 examines the light-curve evolution and colour behaviour, and explores a range of semi-analytic models to interpret the luminosity and temporal evolution of SN 2017ati. Section 4 is devoted to spectroscopic analysis, including a comparison of the spectral characteristics with those of other Type IIb SNe. A detailed discussion is given in Section 5, followed by a summary of the main results in Section 6. In addition, the data reduction procedures are described in Appendix B, the supplementary data tables are compiled in Appendix C, and the supplementary figures are presented in Appendix D.

2. Basic information for SN 2017ati

SN 2017ati (also known as ATLAS17era¹, CSS170303-094957+671059², and Gaia17aiq³) was discovered on 2017 February 6 (MJD= 57790.4) with the Gaia photometric instrument on board the Gaia spacecraft (Delgado et al. 2017), and was subsequently classified as a Type IIb SN by Benetti (2017). The first detection on 2017 February 5 (MJD = 57789.5) yielded an apparent magnitude of $m_V = 17.62 \pm 0.16$ mag (Vega system) on ASAS-SN, slightly earlier than the reported epoch, while the last non-detection on 2017 January 5 (MJD = 57758.5) provided

a limiting apparent magnitude of $m_c = 20.89$ mag in the *cyan* filter (AB system) on ATLAS.

The coordinates of SN 2017ati are RA = $09^{\text{h}}49^{\text{m}}56^{\text{s}}.70$ and Dec = $+67^{\circ}10'59''.56$. The location of SN 2017ati is shown in Fig. D.1. SN 2017ati was initially reported to the Transient Name Server (TNS) as a hostless SN. However, a wider-field inspection revealed that SN 2017ati lies between two galaxies, at projected distances of $36''$ and $76''$ from their respective nuclei. This places SN 2017ati about 10 kpc ($36''$) from the centre of the nearest galaxy, KUG 0946+674. The two galaxies appear to be interacting, and such interaction could have triggered a region of enhanced star formation, which may account for the occurrence of a CCSN at such a remote location from the host galaxy disc (Balakina et al. 2019; Taggart & Perley 2021). We adopt a recessional velocity of $v = 5084 \pm 13 \text{ km s}^{-1}$ (Mould et al. 2000), corresponding to a redshift of $z = 0.01696$ after applying corrections for the effects of the Virgo Cluster, the Great Attractor, and the Shapley Supercluster. These corrections account for the peculiar motions of the Milky Way and other nearby large-scale structures, which would otherwise affect the derived recessional velocity (Marinoni et al. 1998). Assuming a standard cosmological model with $H_0 = 73 \pm 5 \text{ km s}^{-1} \text{ Mpc}^{-1}$, $\Omega_M = 0.27$, and $\Omega_\Lambda = 0.73$ (Spergel et al. 2007), we obtain a luminosity distance of $d_L = 70.80 \pm 5.20 \text{ Mpc}$, corresponding to a distance modulus of $\mu = 34.25 \pm 0.16 \text{ mag}$ for SN 2017ati.

For the interstellar reddening, we use $E(B - V)_{\text{Gal}} = 0.104$ mag (Schlafly & Finkbeiner 2011, $A_V^{\text{Gal}} = 0.322$ mag) for the Galactic reddening component, as derived from the NASA/IPAC Extragalactic Database (NED)⁴, and assume a reddening law with $R_V = 3.1$ (Cardelli et al. 1989). However, the extinction contribution from the host galaxy remains uncertain, but likely negligible given the outer location of the object. We therefore adopt a total reddening of $E(B - V)_{\text{tot}} = 0.104$ mag towards SN 2017ati, acknowledging that this value likely represents a lower limit to the true extinction.

3. Photometry

3.1. Apparent magnitude light curves

We followed the photometric evolution of SN 2017ati for approximately 300 days post-discovery. The resulting optical light curves are shown in Fig. D.2. We estimated the explosion epoch of SN 2017ati using the fireball expansion method. A 2nd-order polynomial fit, Gaussian Process (GP), and Artificial Neural Network (ANN) models were applied to the data obtained within a 20-day interval before and around the *V*-band maximum in flux space (e.g. González-Gaitán et al. 2015; Wang et al. 2024), as shown in the top panel of Fig. D.3. Following this approach, the explosion epoch of SN 2017ati is calculated to be MJD = $57784.5^{+1.4}_{-2.3}$, derived as the average of three independent estimates based on the epoch at which the flux extrapolates to zero. This epoch is adopted as the reference time throughout this paper. To estimate the peak brightness of SN 2017ati, we fitted the *o*-band light curve over a two week interval around maximum using a 2nd-order polynomial fit, GP, and ANN, and the mean of these fits gives $o = 16.17 \pm 0.01$ mag at MJD 57812.0 \pm 0.8, as shown in the bottom panel of Fig. D.3.

After the maximum light, the multi-band light curves of SN 2017ati display an approximately linear decline, particularly pronounced in the *roiz* bands⁵. Notably, variations in the decline

¹ https://atlas.fallingstar.com/?utm_source=chatgpt.com

² <http://nesssi.cacr.caltech.edu/catalina/20170303/1703031670144113388.html>

³ <http://gsaweb.ast.cam.ac.uk/alerts/alert/Gaia17aiq/>

⁴ <https://ned.ipac.caltech.edu>

⁵ The *Gaia* *G*-band photometry, which broadly corresponds to the *r* band, was used in the construction of the *r - i* colour evolution over

Table 1. Decline rates (in mag /100 d) of the multi-band light curves of SN 2017ati.

Filter	γ_{0-50}	γ_{50-160}
<i>B</i>	4.72 ± 0.59	0.97 ± 0.06
<i>g</i>	4.49 ± 0.29	0.96 ± 0.04
<i>V</i>	4.53 ± 0.21	1.31 ± 0.03
Filter	γ_{0-160}	$\gamma_{160-200}$
<i>r/G</i>	1.37 ± 0.01	1.46 ± 0.01
<i>o</i>	2.76 ± 0.04	–
<i>i</i>	1.81 ± 0.02	–
<i>z</i>	1.54 ± 0.02	–

rates appear around 50 days, especially in the *BgV* bands, while the *u*- and *c*-band data are too sparse to provide a reliable estimate. We estimated the post-peak decline slopes in each band through linear fits to the data after maximum, with the results summarized in Table 1. Owing to the noticeable change in the light-curve slope around 50 d in the *BgV* bands, we derived decline rates between peak and 50 d (γ_{0-50}) and between 50 d and 160 d (γ_{50-160}) for these bands, while a single decline rate was measured for the *oiz* bands. In addition, we measured a late-time decline rate for the *r/G* band between 160 and 300 d ($\gamma_{160-300}$). During the early phase, the decline proceeds more rapidly in the bluer bands than in the redder ones. For example, during the early phase, the *g* band declines rapidly at ~ 4.49 mag 100 d $^{-1}$, whereas the *r* band fades more slowly at only ~ 1.37 mag 100 d $^{-1}$. At later phases, the light-curve decline becomes significantly slower, with decline rates approaching that expected from the $^{56}\text{Co} \rightarrow ^{56}\text{Fe}$ radioactive decay of 0.98 mag 100 d $^{-1}$ (e.g. $\gamma_{50-160}(B) \sim 0.97$ mag 100 d $^{-1}$).

3.2. Absolute magnitude light curves

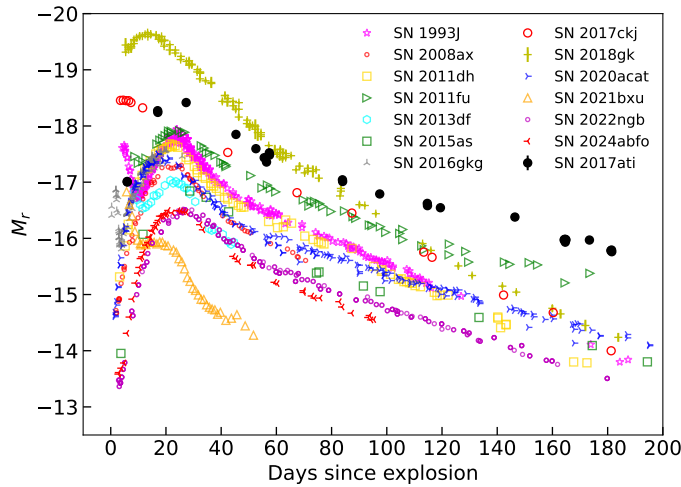


Fig. 1. Absolute *r/G*-band light curve of SN 2017ati compared with other SNe IIb in *r/R*-band. All light curves have been corrected for reddening and shifted according to the distances listed in Table C.2.

In this work, a comparison sample of Type IIb SNe is compiled to serve as a reference for the photometric and spectro-

the range 0 – 0.6 mag (see https://gea.esac.esa.int/archive/documentation/GDR2/Data_processing/chap_cu5pho/sec_cu5pho_calibr/ssec_cu5pho_PhotTransf.html).

scopic analysis of SN 2017ati. The objects included in Appendix Table C.2 are all classified as Type IIb SNe. Within this sample, SN 2008ax exhibits a spectral evolution closely matching that of SN 2017ati, while SN 2017ckj shows a peak luminosity comparable to SN 2017ati but reaches maximum light at an earlier epoch.

Adopting the distance and extinction values from Sect. 2, a second-order polynomial fit to the *r*-band light curve of SN 2017ati yields a peak absolute magnitude of $M_r = -18.48 \pm 0.16$ mag at $\text{MJD} = 57811.1 \pm 0.7$, placing it toward the luminous end of our selected comparison sample. Type IIb SNe generally display comparable luminosities near the radioactive-decay-powered maximum, typically spanning -16.5 to -18 mag (Taddia et al. 2018; Stritzinger et al. 2018a), with the *r/R*-band peak absolute magnitudes of the selected comparison sample provided in Table C.2. A comparison of the absolute *r*-band magnitudes for SN 2017ati and the reference Type IIb SNe is shown in Fig. 1. Within this context, SN 2017ati lies near the upper boundary of the typical luminosity range. SN 2018gk ($M_r = -19.64 \pm 0.24$ mag; Bose et al. 2021) attains an even higher peak luminosity, while SN 2017ckj ($M_r = -18.46 \pm 0.07$ mag; Li et al. 2025a) exhibits a peak magnitude comparable to that of SN 2017ati. However, neither SN 2018gk nor SN 2017ckj exhibits a light curve shape similar to that of SN 2017ati, whereas SN 2011fu does (apart from the initial bump) but is slightly fainter. In contrast, SN 2021bxu does not show a distinct peak but exhibits a plateau at a mostly comparable epoch ($M_r \sim -15.93$ mag; Desai et al. 2023), appearing significantly fainter.

In contrast, the standard radioactive-decay framework successfully accounts for the light curves of typical Type IIb SNe, but it fails to reproduce the observed properties of energetic SNe Ic-BL. Specifically, it cannot simultaneously explain their high peak luminosities and their late-time photometric evolution. For luminous events such as SN 2017ati, which exceed the brightness of ordinary Type IIb SNe, we therefore consider the possibility of an additional energy source contributing to the observed luminosity.

3.3. Colour evolution

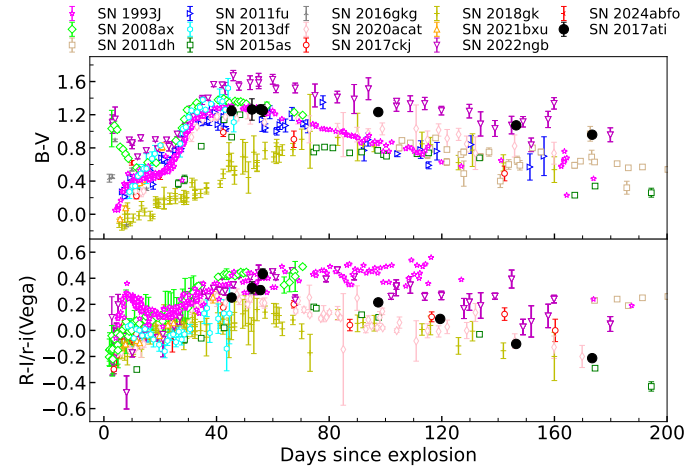


Fig. 2. Colour evolution of SN 2017ati, compared to a sample of SNe IIb. *Upper panel:* $B - V$ colour evolution. *Lower panel:* $(R - I)$ or $(R - i)$ colour evolution. The colour curves are corrected for both Galactic and host galaxy extinction.

The intrinsic colour evolution of SN 2017ati is presented together with the comparison Type IIb sample, with all colour curves corrected for reddening using the parameters provided in Table C.2. During the early phases after the explosion, the $B - V$ colour of SN 2017ati is missing, whereas the comparison Type IIb sample exhibits a rising trend. Between 40 and 60 days after the explosion, the $B - V$ colour of SN 2017ati remains at around 1.26 mag. Most comparison Type IIb SNe reach their peak colour in this interval, except SN 2018gk, which continues to redden. From 90 to 180 days after the explosion, the $B - V$ colour of SN 2017ati gradually decreases from 1.23 ± 0.04 mag to 0.96 ± 0.03 mag. Overall, the $B - V$ colour evolution of SN 2017ati broadly traces the behaviour seen in previously studied Type IIb SNe (see the top panel in Fig. 2).

For SN 2017ati, the $r - i$ colour evolution closely resembles that observed in SNe 2015as, 2018gk, and 2020acat, showing an initial rise to a well-defined peak followed by a rapid decline, suggesting a broadly comparable physical evolution (see the bottom panel in Fig. 2). Owing to the lack of very early-time observations, the initial shock-cooling phase cannot be directly constrained. During the photospheric phase, between ~ 40 and 60 d after the explosion, the $r - i$ colour becomes progressively redder and reaches a maximum of 0.43 ± 0.04 mag at about 56 d, which is consistent with continued ejecta expansion and photospheric cooling, causing the spectral energy distribution to shift toward longer wavelengths. At later epochs, between approximately 90 and 180 d after the explosion, the $r - i$ colour of SN 2017ati declines rapidly, showing behaviour similar to that observed in SNe 2015as, 2020acat, and 2018gk. In contrast, SNe 1993J, 2011dh, and 2017ckj do not display a comparable decrease at similar phases, but instead maintain an approximately constant $R - I / r - i$ colour.

3.4. Pseudo-bolometric light curves

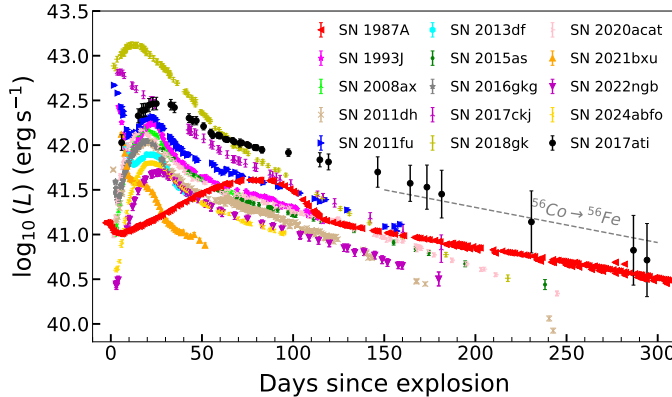


Fig. 3. Comparison of the pseudo-bolometric light curve of SN 2017ati with those of SN 1987A and other Type IIb SNe. The grey dashed line illustrates the expected slope of the light curve under the assumption that all energy from ^{56}Co decay is fully thermalized by the ejecta.

Using the available optical photometry and the SuperBol⁶ code (Nicholl 2018), a pseudo-bolometric light curve of SN 2017ati was constructed from the optical bands. For epochs with missing data in certain filters, values were estimated by extrapolating from the available measurements. For a consistent comparison, pseudo-bolometric light curves of the other SNe

were constructed using the U/u to I/i bands, with filters lacking sufficient data not included in the fitting procedure.

The pseudo-bolometric light curve of SN 2017ati, derived through blackbody fits, is compared with those of other Type IIb SNe summarised in Table C.2 and is shown in Fig. 3. SN 2017ati exhibits a peak luminosity of around $L \sim 3.00 \times 10^{42}$ erg s $^{-1}$, which is lower than those of SNe 2017ckj ($L \sim 6.65 \times 10^{42}$ erg s $^{-1}$) and 2018gk ($L \sim 1.43 \times 10^{43}$ erg s $^{-1}$), yet still relatively bright compared with other SNe IIb in the sample. The rise time of SN 2017ati is approximately 29.1 d, in close agreement with the values determined for SNe 2008ax, 2022ngb, and 2024abfo (Pastorello et al. 2008; Zhao et al. 2025; Reguitti et al. 2025). In contrast, events classified as Type IIb such as SNe 1993J, 2011fu, 2013df, and 2016gkg present pronounced double-peaked profiles, indicating that contribution from an expanded progenitor envelope is more significant in these cases than in SN 2017ati.

Based on the bolometric luminosity, an estimate of the ^{56}Ni mass synthesised in SN 2017ati is derived. For hydrogen-rich SNe, including SN 2017ati, determining the fraction of luminosity contributed by ^{56}Ni near peak is challenging, as hydrogen recombination can lead to uncertain estimates (Charalampopoulos et al. 2025). Using the peak luminosity of SN 2017ati and adopting the Arnett rule (Arnett 1982), the ^{56}Ni mass is evaluated to be $\sim 0.40 M_{\odot}$. This value should be treated as an upper limit.

For SE SNe, Clocchiatti & Wheeler (1997) introduced a parametrised description of the luminosity decline at late phases:

$$L(t) = L_0(t) \times \left[1 - e^{-(T_0/t)^2} \right], \quad (1)$$

where T_0 denotes the characteristic timescale governing the transition from complete to incomplete trapping of the radioactive decay energy. Assuming homologous expansion with spherical geometry and radioactive material located centrally, Jerkstrand et al. (2012) derived the theoretical luminosity for the case in which the energy released by the decay of ^{56}Co is fully trapped, expressed as

$$L_0(t) = 9.92 \times 10^{41} \frac{M_{\text{Ni}}}{0.07 M_{\odot}} (e^{-t/111.4} - e^{-t/8.8}) \text{ erg s}^{-1}, \quad (2)$$

where M_{Ni} denotes the ejected mass of ^{56}Ni . Using this formulation and performing an Markov chain Monte Carlo (MCMC) fit, the ^{56}Ni mass for SN 2017ati is determined to be $0.29^{+0.05}_{-0.04} M_{\odot}$, along with a characteristic timescale of $T_0 = 225.8^{+58.4}_{-45.9}$ d. For SE SNe, the characteristic timescale is typically in the range $T_0 \approx 80 - 140$ d (Sharon & Kushnir 2020). The unusually large value of T_0 derived for SN 2017ati may reflect the presence of additional energy sources beyond radioactive decay or a relatively massive progenitor star.

A comparison with the tail luminosity of SN 1987A, for which $M(^{56}\text{Ni})_{\text{SN} 1987\text{A}} = 0.075 \pm 0.005 M_{\odot}$ (Arnett 1996), yields a value of $0.47 \pm 0.13 M_{\odot}$ for SN 2017ati. These estimates of the ^{56}Ni mass for SN 2017ati are relatively high compared with values usually found for SNe IIb, suggesting that additional energy input beyond radioactive heating may contribute to powering the light curve. All estimated values of the ^{56}Ni mass, together with the ^{56}Ni mass inferred from the models applied in Sect. 3.5, are summarised in Table C.3.

3.5. Modelling the multi-band light curves with MOSFiT

Given that SN 2017ati exhibits luminosity differences compared with previously studied SNe IIb, we employed the publicly avail-

⁶ <https://github.com/mnicholl/superbol>

able Modular Open-Source Fitter for Transients (MOSFiT⁷; Guillotin et al. 2018) to model the multi-band light curves and explore potential powering mechanisms. This tool takes multi-band photometry as input and enables the use of prior distributions for model parameters, providing constraints on alternative energy contributions. A MCMC approach is used in MOSFiT to explore the parameter space associated with each built-in model, resulting in a best-fitting light curve and corresponding parameter constraints.

In this work, three energy-input scenarios available in MOSFiT are examined to interpret the observed luminosity evolution of SN 2017ati.

- ^{56}Ni decay: luminosity arises solely from the decay chain of ^{56}Ni and ^{56}Co , adopting the standard treatment for Type I Ib events (Nadyozhin 1994).
- ^{56}Ni decay plus CSM interaction: luminosity is powered both by radioactive decay and ejecta interaction with circumstellar material, following the model of Chatzopoulos et al. (2013).
- ^{56}Ni decay plus magnetar: this model adopts the radioactive framework above and introduces an additional contribution from a magnetar central engine, following the formulation of Nicholl et al. (2017).

For every scenario, MOSFiT is applied with an MCMC inference framework, adopting the PHOTOSPHERES.TEMPERATURE_FLOOR prescription for the photospheric evolution, following the treatment in Nicholl et al. (2017). Throughout the fitting process, a uniform opacity for UVOIR emission of $\kappa = 0.195 \text{ cm}^2 \text{ g}^{-1}$ is utilised, following the value recommended by Nagy (2018).

The results of the ^{56}Ni decay model, together with the corresponding corner plot, are displayed in Fig. D.4 of Appendix D. The fitted parameters are listed in Table C.4. For the ^{56}Ni decay model, seven free parameters are employed, yielding an ejecta mass of $M_{\text{ej}} = 1.70_{-0.38}^{+0.44} \text{ M}_\odot$, a ^{56}Ni mass of $M_{^{56}\text{Ni}} = 0.37_{-0.10}^{+0.07} \text{ M}_\odot$, a gamma-ray opacity of $\kappa_\gamma = 0.06_{-0.01}^{+0.03} \text{ cm}^2 \text{ g}^{-1}$, a temperature floor of $T_{\text{min}} = 4.47_{-0.20}^{+0.21} \times 10^3 \text{ K}$, an ejecta velocity of $v_{\text{ej}} = 3.63_{-0.24}^{+0.26} \times 10^3 \text{ km s}^{-1}$, and an additional uncertainty term of $\sigma = 0.37_{-0.02}^{+0.03}$. The inferred explosion epoch from the model is $t_{\text{exp}} = -33.97_{-1.03}^{+1.55} \text{ days}$ (measured relative to the first detection), which is earlier than the explosion time estimated from our analysis by 28.97 days.

It is evident that a framework based solely on ^{56}Ni radioactive decay fails to reproduce the multi-band light curves of SN 2017ati. Significant discrepancies emerge at early phases, where the observed flux cannot be matched by the model. Although the corner plot suggests statistical convergence, the inferred explosion epoch is markedly earlier than our estimated value, the ^{56}Ni mass is higher than that commonly deduced for SNe I Ib, and an extra uncertainty of $\sigma = 0.37$ is required to maintain the fitting quality. These limitations indicate that this model does not offer a physically reliable representation of the radiative evolution of SN 2017ati.

We subsequently examined a model combining ^{56}Ni radioactive heating with a contribution from CSM interaction. The resulting fit, along with the corresponding corner plot, are shown in Fig. D.5, and the fitted parameters are summarised in Table C.4. Although clear signatures of CSM interaction are not evident in either the spectra or light curves of SN 2017ati, the possibility of interaction with surrounding material cannot be entirely excluded, particularly in the case of a low-density CSM (Dessart &

Hillier 2022; Peng et al. 2026) and in the absence of ultraviolet observations. This composite framework provides an improved reproduction of the multi-band light curves of SN 2017ati, particularly at early phases and near the peak luminosity. However, the fit demands an ejecta mass of $M_{\text{ej}} = 4.90_{-0.53}^{+0.72} \text{ M}_\odot$, which lies outside the range typically associated with SNe I Ib, together with a markedly elevated ^{56}Ni mass, which is $0.74_{-0.15}^{+0.20} \text{ M}_\odot$. Overall, the best-fitting values of these parameters deviate significantly from realistic expectations, making difficult to regard the model as a credible description of SN 2017ati.

We further explored a model in which the ^{56}Ni radioactive heating is supplemented by energy input from a magnetar. This scenario provides a markedly improved reproduction of the multi-band light curves of SN 2017ati, with the scatter reduced to $\sigma = 0.17_{-0.02}^{+0.01}$. The resulting parameters are also more consistent with those commonly inferred for SNe I Ib. In this framework, nine free parameters are employed. The best-fitting model and the corresponding corner plot are shown in Fig. D.6, and the inferred parameters are listed in Table C.4. The ^{56}Ni decay plus magnetar fit yields a magnetic field strength of $B = 13.2_{-4.3}^{+4.6} \times 10^{14} \text{ G}$, together with an initial spin period of $P_{\text{spin}} = 28.2_{-6.3}^{+2.7} \text{ ms}$. The inferred ejecta mass is $M_{\text{ej}} = 1.82_{-0.59}^{+0.53} \text{ M}_\odot$ and is accompanied by a ^{56}Ni mass of $M_{^{56}\text{Ni}} = 0.21_{-0.12}^{+0.08} \text{ M}_\odot$. The fit additionally requires a gamma-ray opacity of $\kappa_\gamma = 0.33_{-0.05}^{+0.12} \text{ cm}^2 \text{ g}^{-1}$, a temperature floor of $T_{\text{min}} = 4.57_{-0.10}^{+0.11} \times 10^3 \text{ K}$, and an ejecta velocity of $v_{\text{ej}} = 7.24_{-0.64}^{+0.70} \times 10^3 \text{ km s}^{-1}$. The model implies an explosion epoch of $t_{\text{exp}} = -7.36_{-0.99}^{+1.04} \text{ d}$ relative to the first detection, which is close to the independently estimated value of -5.0 d , and adopts a neutron star mass of $M_{\text{ns}} = 1.5 \text{ M}_\odot$.

These physical parameters derived from the modelling of SN 2017ati are broadly consistent with expectations for SNe I Ib. The inferred ejecta mass of $M_{\text{ej}} = 1.82_{-0.59}^{+0.53} \text{ M}_\odot$ lies within the range of $\sim 1.7 - 5.2 \text{ M}_\odot$ obtained for SE-SNe from radiative-transfer model grids (Dessart et al. 2016). The ^{56}Ni mass of $M_{^{56}\text{Ni}} = 0.21_{-0.12}^{+0.08} \text{ M}_\odot$ falls within the distribution observed for SNe I Ib, but is close to the upper end of the reported range of $0.03 - 0.28 \text{ M}_\odot$ (Anderson 2019; Meza & Anderson 2020). The ejecta velocity of $v_{\text{ej}} = 7.24_{-0.64}^{+0.70} \times 10^3 \text{ km s}^{-1}$ is consistent with the spectral velocities measured in Sect. 4.2. The measured magnetic field strength of $B = 13.2_{-4.3}^{+4.6} \times 10^{14} \text{ G}$ significantly exceeds the typical range of magnetic fields observed in newly born neutron stars and instead falls within the characteristic range for magnetars ($3 \times 10^{14} - 10^{15} \text{ G}$; Beniamini et al. 2019). Compared with the other models discussed above, a framework combining ^{56}Ni radioactive heating with additional energy input from a magnetar yields parameter values that provide a more physically plausible match to the observed properties for SN 2017ati.

4. Spectroscopy

4.1. Spectral sequence

The spectroscopic campaign of SN 2017ati covers phases from $+27.3 \text{ d}$ to $+148.4 \text{ d}$ after the explosion, commencing near maximum light and extending well into the nebular regime. The observational log is listed in Table C.1, and the spectral sequence is shown in Fig. 4, illustrating the temporal evolution over the photospheric and the early nebular stages.

The earliest spectrum of SN 2017ati was secured near the optical peak, and the initial five spectra (from $+27.3 \text{ d}$ to $+55.5 \text{ d}$) reveal persistent and pronounced H and He signatures. Prominent lines of $\text{H}\alpha \lambda 6563$, $\text{H}\beta \lambda 4861$, $\text{H}\gamma \lambda 4340$, $\text{He I } \lambda\lambda 5876, 7065$, and $\text{O I } \lambda 7774$ are clearly detected and ex-

⁷ <https://mosfit.readthedocs.io/en/latest/index.html>

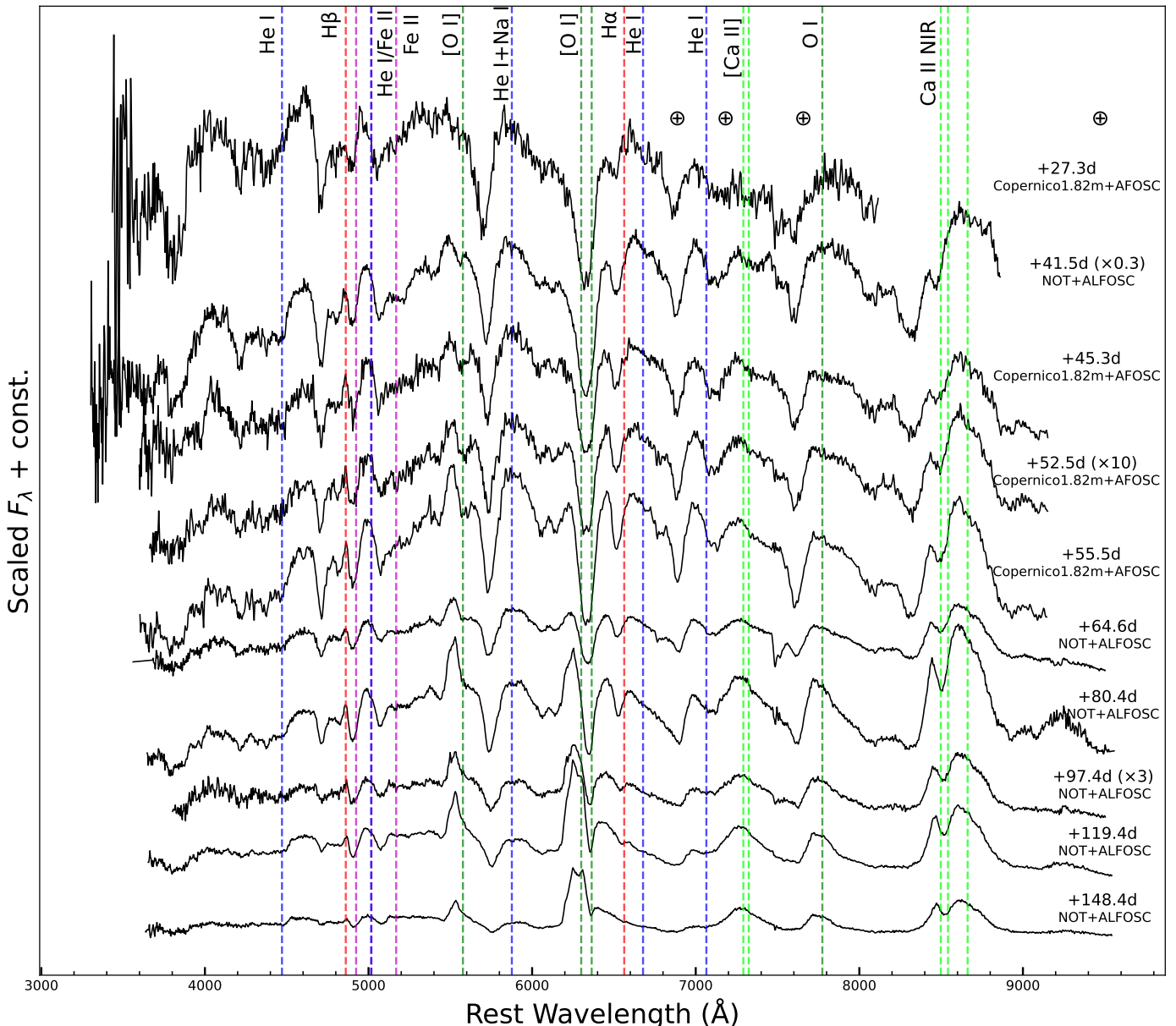


Fig. 4. Optical spectral evolution of SN 2017ati from +27.3 days to +148.4 days since the explosion. The spectra have been corrected for reddening and redshift, and vertically shifted for better visualization. The epochs are indicated to the right of each spectrum. The positions of major telluric absorption lines are denoted by the \oplus symbol.

hibit a gradual increase in strength as the ejecta cools and recedes. A detailed analysis of this behaviour is presented in Sect. 4.2.

As time progresses, nebular signatures such as $[O I] \lambda\lambda 6300, 6364$ and $[Ca II] \lambda\lambda 7291, 7324$, which are characteristic of the nebular phase, become clearly visible from +64.6 d. During this phase, the $H\alpha$ emission exhibits a noticeable decline, whereas the $[O I] \lambda\lambda 6300, 6364$ feature continues to strengthen. In the spectrum at +148.4 d, SN 2017ati shows a small bump on the redshifted side of the $[O I]$ doublet, closely resembling that observed in SN 1993J. This excess may be associated with contributions from $H\alpha$, $He I$, and $[N II]$ (Patat et al. 1995; Houck & Fransson 1996), is discussed further in Sect. 4.4.1. The $Ca II$ NIR triplet ($\lambda\lambda 8498, 8542, 8662$) is already detected in emission at +41.5 d and remains persistently strong at later epochs.

4.2. Spectra line profile and velocity evolution

The evolution of line profiles for $He I \lambda\lambda 5016, 5876$, $O I \lambda 7774$, $[O I] \lambda 6300$, $[Ca II] \lambda\lambda 7291, 7324$, and the $Ca II$ NIR triplet in spectra of SN 2017ati is shown in Fig. 5. In the earliest spectrum of SN 2017ati at +27.3 d, the $He I$ and $O I$ lines exhibit clear broad P Cygni profiles, indicating outwardly expanding ejecta and the presence of these elements in rapidly moving material. With time, the blueshift of the $He I$ absorption features decreases gradually, from about $-10,000 \text{ km s}^{-1}$ for $He I \lambda 5876$ at early phases to roughly $-5,000 \text{ km s}^{-1}$ at +148.4 d. This behaviour is naturally explained by the recession of the line-forming region from the fast, outer ejecta to progressively deeper layers with lower expansion velocities, as the ejecta expand and become increasingly optically thin (Dessart & Hillier 2005). It is noteworthy that in the earliest five spectra, the $He I \lambda\lambda 5016, 5876$ and $O I \lambda 7774$ lines exhibit a pronounced boxy morphology from 27.3 d

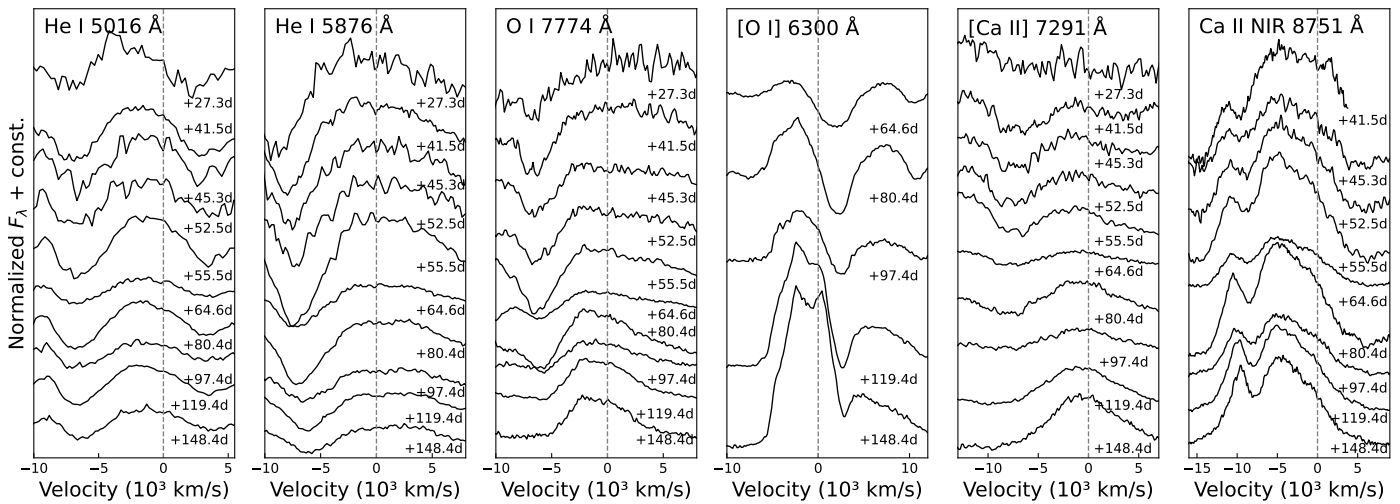


Fig. 5. Line profiles of He I, O I, [O I], [Ca II] and Ca II NIR within the spectra of SN 2017ati. The dashed lines indicate the velocities corresponding to the rest wavelengths of the emission lines at $\lambda\lambda 5016, 5876, 7774, 6300, 7291$, and 8751 . The epoch of each spectrum is given in the rest frame, relative to the estimated explosion date.

Table 2. Velocity measurements for the main absorption minimum with uncertainties (in km/s).

Phase ^a [days]	H α [km s $^{-1}$]	H β [km s $^{-1}$]	He I $\lambda 5876$ [km s $^{-1}$]	Fe II $\lambda 5018$ [km s $^{-1}$]
+27.3	11220(370)	9070(300)	9110(380)	7680(380)
+41.5	11030(250)	9270(200)	8110(230)	7140(160)
+45.3	10851(240)	9290(240)	7750(270)	6550(330)
+52.5	10720(220)	9540(200)	7410(270)	7050(370)
+55.5	10520(230)	9220(220)	7280(310)	6970(470)
+64.6	10220(180)	9140(200)	7090(240)	6780(240)
+80.4	9870(190)	9040(210)	6790(210)	6790(220)
+97.4	—	—	6360(260)	6630(230)

^a Phases are calculated relative to the explosion epoch (MJD = 57784.5) in the reference frame of the observer.

to 52.5 d, as illustrated in the first three panels of Fig. 5. This boxy appearance is not seen in the Balmer features, which instead maintain standard P Cygni profiles over the same epochs.

The boxy structure of the He I and O I lines suggests that their emission originates from a confined region of the ejecta, occupying a narrow velocity interval of approximately $-5,000$ km s $^{-1}$ to 0 km s $^{-1}$. Such a configuration implies a stratified distribution in which the bulk of the intermediate-mass elements reside within a well-defined shell rather than being efficiently mixed into deeper layers or the fast outer ejecta. The absence of a similar morphology in the H features indicates that hydrogen is present at different velocities without forming a comparably sharp shell, consistent with a partially stripped envelope. This stratified structure also provides a natural explanation for the later emergence of the double-peaked [O I] $\lambda\lambda 6300, 6364$ emission, typically associated with an oxygen-rich, radially confined or asymmetric zone.

The spectrum of SN 2017ati at +64.6 d already exhibits a weak [O I] $\lambda\lambda 6300, 6364$ emission component, which subsequently increases in strength with time. In SNe IIb, the [O I] emission becomes progressively more prominent toward late phases, as observed in well-studied events such as SNe 1993J, 2008ax, and 2011fu (Richmond et al. 1994; Pastorello et al. 2008; Tsvetkov et al. 2009; Taubenberger et al. 2011; Fang

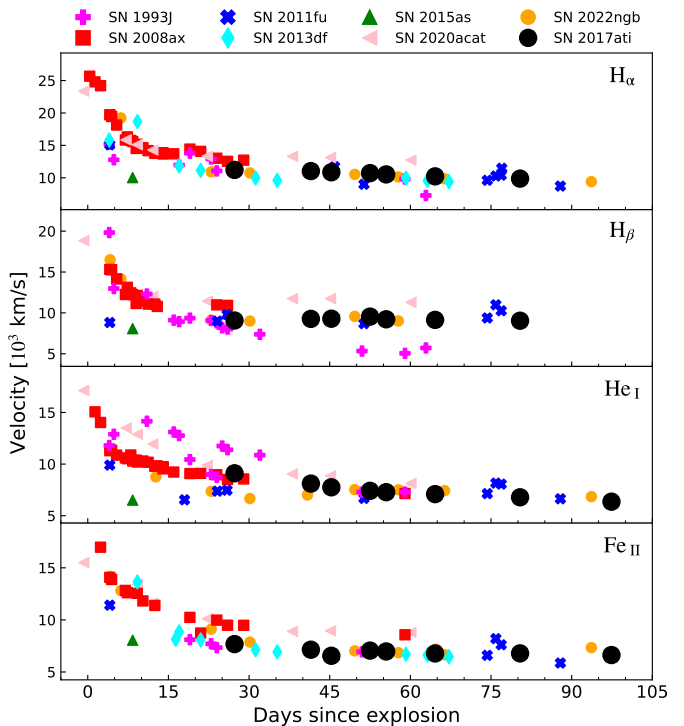


Fig. 6. Evolution of the line velocities for H α $\lambda 6563$ \AA , H β $\lambda 4861$ \AA , He I $\lambda 5876$ \AA , and Fe II $\lambda 5018$ \AA . SN 2017ati and other comparisons are marked with different symbols. The measured values and uncertainties for SN 2017ati are listed in Table 2.

et al. 2022). This behaviour reflects the increasing contribution of the energy deposited in the oxygen-rich inner ejecta as the photosphere recedes, enabling forbidden-line emission to emerge under low-density, homologously expanding conditions. In the final spectrum of SN 2017ati at +148.4 d, the [O I] $\lambda\lambda 6300, 6364$ feature develops a clear double-peaked structure with an additional red-side excess, which is discussed in detail in Sect. 4.4.1. During this period, the [O I] $\lambda\lambda 6300, 6364$ exhibits a pronounced blueshift that gradually diminishes, de-

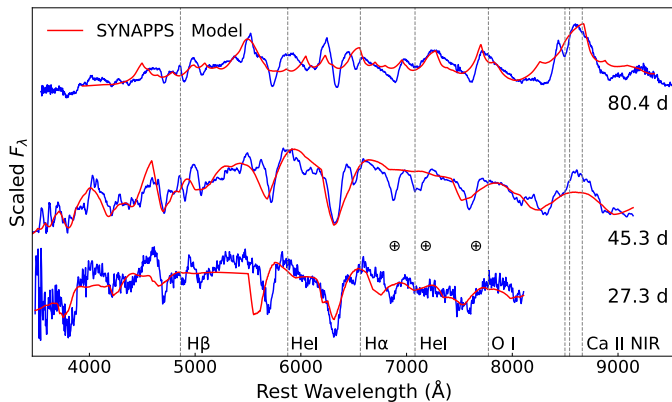


Fig. 7. Comparison between observed spectra and SYNAPPS models, together with line identifications, for SN 2017ati at three epochs. The spectra are corrected for extinction and redshift.

clining from nearly $-5,000 \text{ km s}^{-1}$ at $+64.6 \text{ d}$ to approximately $-2,500 \text{ km s}^{-1}$ by $+148.8 \text{ d}$.

As the spectra evolve, the $[\text{Ca II}] \lambda\lambda 7291, 7324$ emission lines of SN 2017ati display an approximately symmetric profile and gradually increase in strength with time. By contrast, the near-infrared Ca II triplet is already prominent at early epochs and shows a pronounced blueshift. This contrasting behaviour can be understood in terms of the different formation conditions of permitted and forbidden calcium transitions. The Ca II near-infrared triplet originates predominantly in the dense, optically thick outer ejecta at early phases, where resonance scattering and line opacity favour blueshifted absorption and emission from the approaching hemisphere. As the ejecta expand and the density decreases, the line-forming region recedes to deeper layers and the forbidden $[\text{Ca II}]$ transitions become increasingly efficient, giving rise to stronger and more symmetric emission profiles that trace the more globally distributed calcium-rich material.

To further quantify the kinematic evolution implied by these spectral changes, SN 2017ati is analysed through measurements of spectral line expansion velocities. Gaussian profile fitting is applied to the principal absorption minima in the spectra of SN 2017ati to derive the corresponding velocities. The analysis concentrates on $\text{H}\alpha$, $\text{H}\beta$, $\text{He I} \lambda 5876$, and $\text{Fe II} \lambda 5018$. The resulting velocity evolution is compared with that of a representative sample of SNe IIb. The temporal behaviour of these line velocities for SN 2017ati and the comparison objects is shown in Fig. 6, while the measured values and associated uncertainties for SN 2017ati are listed in Table 2.

The velocity evolution of SN 2017ati broadly follows the trends observed in the majority of Type IIb SNe events included in the comparison sample. Owing to the absence of early-time spectra, the initial line velocities of SN 2017ati cannot be constrained. At intermediate and late phases, the H-line velocity of SN 2017ati occupies an intermediate range among Type IIb events, with values similar to those measured in SNe 2011fu, 2013df, and 2022ngb, lower than those observed in SN 2020acat, and higher than those inferred for SN 1993J, as illustrated in the two upper panels of Fig. 6. For SN 2017ati, the $\text{H}\alpha$ velocity shows a gradual decline from $\sim 11,220 \text{ km s}^{-1}$ at $+27.3 \text{ d}$ after the explosion to $\sim 9,870 \text{ km s}^{-1}$ at $+80.4 \text{ d}$. In contrast, the $\text{H}\beta$ velocity in SN 2017ati increases from $\sim 9,070 \text{ km s}^{-1}$ at $+27.3 \text{ d}$ to a peak of $\sim 9,540 \text{ km s}^{-1}$ at $+52.5 \text{ d}$, before declining to $\sim 9,040 \text{ km s}^{-1}$ by $+80.4 \text{ d}$. The evolution of $\text{H}\beta$ is likely similar to that of $\text{H}\alpha$, although $\text{H}\beta$ lies in a more crowded spectral region, which results in differences in their measured velocities.

At later epochs, the H features in SN 2017ati fade from the spectra, preventing further reliable velocity measurements.

A comparable decline is seen in the He I and Fe II features of SN 2017ati, with their velocities broadly consistent with those measured in the representative Type IIb SNe. The $\text{He I} \lambda 5876$ velocity decreases from $\sim 9,110 \text{ km s}^{-1}$ at $+27.3 \text{ d}$ to $\sim 6,360 \text{ km s}^{-1}$ by $+97.4 \text{ d}$, while the $\text{Fe II} \lambda 5018$ line exhibits a more gradual evolution, declining from $\sim 7,680 \text{ km s}^{-1}$ at $+27.3 \text{ d}$ to $\sim 6,630 \text{ km s}^{-1}$ at $+97.4 \text{ d}$. The velocities inferred from He I and Fe II lines are systematically lower and exhibit a smoother temporal evolution than those of the Balmer features (see the bottom two panels of Fig. 6), consistent with their formation in deeper ejecta layers as the line-forming region recedes. This behaviour has been previously reported in SE-SNe (e.g. Matheson et al. 2000; Branch et al. 2002).

Because hydrogen and helium lines do not reliably trace the photospheric velocity, the $\text{Fe II} \lambda 5018$ line is commonly adopted as a photospheric proxy, as it forms in deeper layers of the ejecta (Dessart & Hillier 2005). Following this approach, the photospheric velocity of SN 2017ati is estimated from the $\text{Fe II} \lambda 5018$ absorption measured at -0.2 d relative to the α -band maximum (corresponding to $+27.3 \text{ d}$ after the explosion), yielding a value of $\sim 7,680 \text{ km s}^{-1}$. This estimate is in good agreement with the ejecta velocity inferred in Sect. 3.5 using MOSFiT within the radioactive-decay plus magnetar central-engine framework, which gives $v_{\text{ej}} = 7.24^{+0.70}_{-0.64} \times 10^3 \text{ km s}^{-1}$. The consistency between these independent estimates supports the physical credibility of the parameters derived from the model.

To identify the ions contributing to the photospheric spectra of SN 2017ati, synthetic spectra were computed with SYNAPPS⁸ (Thomas et al. 2011; Thomas 2013). For SN 2017ati, the synthetic calculations were constructed to reproduce the observed spectra at epochs of $+27.3$, $+45.3$, and $+80.4 \text{ d}$ after the explosion. The synthetic spectra include contributions from a selected set of atomic species, including H I , He I , O II , Ti II , Sc II , Ca II , Fe II , and Ba II , which collectively reproduce the dominant absorption and emission features observed in the spectra. The corresponding SYNAPPS models illustrating the line identifications at three representative epochs for SN 2017ati are shown in Fig. 7. Although the SYNAPPS model does not reproduce the observed line profiles perfectly, particularly at wavelengths shorter than 5500 \AA , it robustly identifies the dominant contributing species, including $\text{H}\alpha$, He I , O I , and Ca II , while the depression near 7000 \AA can be attributed to residual telluric absorption.

4.3. Comparison of Type IIb SNe spectra

To place SN 2017ati in the context of typical SNe IIb, including SNe 1993J, 2008ax, 2011dh, and 2011fu, its spectra are compared with those of well-studied objects observed at similar phases⁹ (see Fig. 8). Prominent spectral features are identified and labelled in each panel. For consistency and to facilitate a clearer comparison of line profiles and relative strengths, all spectra have been normalized. Each spectrum was corrected for both redshift and line-of-sight extinction.

The spectrum of SN 2017ati at 27.3 d after the explosion is compared with those of other SNe IIb observed at a similar epoch, as shown in the upper panel of Fig. 8. Although P Cygni

⁸ <https://github.com/rctthomas/es/>

⁹ Spectra of the comparison objects were obtained from the WISERep database (<https://www.wiserep.org/>, Yaron & Gal-Yam 2012; Goldwasser et al. 2022).

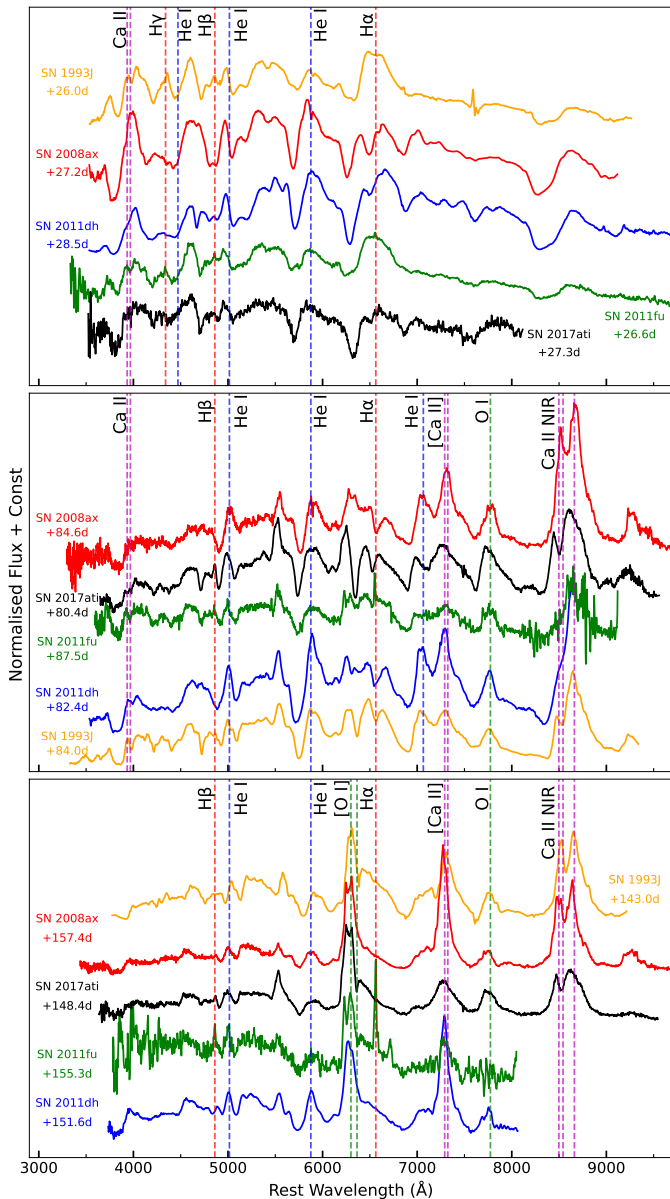


Fig. 8. Comparisons of the spectra of SN 2017ati with other Type Iib events. Key spectral lines are highlighted with corresponding labels.

profiles of $H\alpha$ are present in all spectra at this phase, their overall strengths and velocity extents vary among different SNe Iib. The central absorption feature embedded within the $H\alpha$ emission profile of SN 2017ati is clearly detected and closely resembles that seen in SNe 1993J, 2008ax, and 2011dh. This component is likely associated with the P Cygni absorption of the $He I \lambda 6678$ line, while a comparable feature is not evident in the spectra of SN 2011fu. The $He I$ P Cygni features in SN 2017ati and the other SNe Iib in the comparison sample show clear blueshifts. At this epoch, the overall spectral morphology of SN 2017ati shows a particularly close resemblance to that of SNe 2008ax and 2011dh.

The spectrum of SN 2017ati at +80.4 d, shown in the middle panel of Fig. 8, is compared with a subset of SNe Iib observed at similar phases. At this epoch, SN 2017ati shows a clearly detected, single-peaked $[O I] \lambda\lambda 6300, 6364$ profile together with a still-prominent $H\alpha$ P Cygni feature. SN 2017ati exhibits significantly enhanced $[Ca II] \lambda\lambda 7291, 7324$ emission

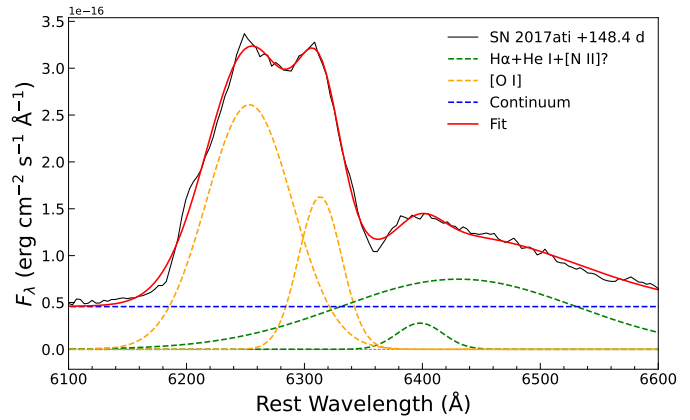


Fig. 9. Multi component Gaussian fit to the $[O I] \lambda\lambda 6300, 6364$ doublet in the nebular-phase spectrum of SN 2017ati at +148.4 d (6100 – 6600 Å).

along with the presence of additional metal lines, including $Mg I \lambda 4571$, $Fe II \lambda\lambda 4924, 5018, 5169$, and $O I \lambda\lambda 7772, 7774$, indicating a progressive transition towards a nebular-dominated spectral regime. Overall, the spectrum of SN 2017ati at this phase closely resembles that of SN 1993J and broadly matches the general properties of the other comparison SNe Iib.

The nebular-phase spectrum of SN 2017ati at +148.4 d post-explosion, shown in the lower panel of Fig. 8, is compared with a selection of Type Iib SNe, highlighting the late-time spectral evolution during the nebular phase. At this stage, the spectra of SN 2017ati are dominated by prominent nebular emission features, including $[O I] \lambda\lambda 6300, 6364$, $[Ca II] \lambda\lambda 7291, 7324$, and the $Ca II$ NIR triplet at $\lambda\lambda 8498, 8542, 8662$, all of which are well developed, while $H\alpha$ has largely faded. The spectra of SN 2017ati at this phase show a strong similarity to those of SNe 1993J and 2008ax, with the $[O I] \lambda\lambda 6300, 6364$ feature exhibiting a double-peaked profile, reminiscent of SNe 2008ax and 2011fu. A detailed discussion of the nebular-phase spectra is provided in Sect. 4.4.

4.4. Nebular spectra

Nebular-phase spectra of CCSNe are commonly employed to infer progenitor and explosion properties. These spectra, obtained once the ejecta become optically thin, provide direct insights into the composition, distribution, and kinematics of the inner layers of the SN. In particular, analysis of nebular emission lines, such as $[O I]$ and $[Ca II]$, allows for the estimation of oxygen mass, assessment of line-profile asymmetries, and comparison with theoretical explosion models. Together, these diagnostics can be used to estimate the zero-age main-sequence (ZAMS) mass of the progenitor and to explore details of the explosion geometry and the nucleosynthesis (Fang et al. 2024).

4.4.1. Nebular $[O I]$ line profile

During the nebular phase, SN 2017ati exhibits a nearly symmetric double-peaked profile in $[O I] \lambda\lambda 6300, 6364$, distinguishing it from SNe 1993J and 2011dh. Double-peaked $[O I]$ emission lines are relatively common in late-time spectra of SE-SNe, as seen for example in SNe 2008ax and 2011fu, and are often interpreted as arising from oxygen distributed in a ring-like configuration, with the line of sight approximately aligned with the plane of the ring (Mazzali et al. 2005, 2008; Tanaka et al. 2009;

Maurer et al. 2010). An alternative explanation attributes the apparent double peaks to the intrinsic $[\text{O I}] \lambda\lambda 6300, 6364$ doublet, whose line ratio evolves from unity at early times to 3:1 in the optically thin regime at late epochs (Li & McCray 1992; Taubenberger et al. 2009; Milisavljevic et al. 2010). Based on the subsequent analysis of the nebular spectrum of SN 2017ati, this interpretation is favoured.

We performed a continuum-subtracted spectral fit of SN 2017ati at +148.4 d over 6100 – 6600 Å, modelling the $[\text{O I}]$ doublet with two Gaussians and the small red-side bump with two additional Gaussians (see Fig. 9). In this spectrum, SN 2017ati exhibits a distinct red-side excess similar to that seen in SN 1993J, which cannot be reproduced by the $[\text{O I}]$ doublet alone, indicating additional line contributions. Old nebular-phase modelling showed that non-thermal excitation by radioactive decay products can sustain $\text{H}\alpha$ emission at late epochs (Kozma & Fransson 1998; Houck & Fransson 1996). Modern nebular spectral synthesis models for SE-SNe further suggest that the $[\text{O I}]$ region can be contaminated by $\text{H}\alpha$, He I , and $[\text{N II}] \lambda\lambda 6548, 6583$, particularly in Type IIb events where residual hydrogen is present (Jerkstrand et al. 2015b; Dessart et al. 2021). Comparative studies indicate that such red-side excess emission is common among SE-SNe and does not uniquely trace large-scale ejecta asymmetries, but is consistent with compositional mixing between hydrogen-rich and metal-rich layers (Taubenberger et al. 2009).

The apparent symmetry and the significant blueshift observed (~ 2240 km/s) in the $[\text{O I}]$ doublet of SN 2017ati can largely be attributed to line blending and non-thermal excitation effects, similar to those identified in SN 1993J. Nevertheless, a non-spherical explosion leading to an asymmetric oxygen distribution cannot be entirely excluded, analogous to the ejecta geometries inferred for SN 2008ax (Mazzali et al. 2005; Maeda et al. 2007; Valenti et al. 2011; Kumar et al. 2022). The fitted $[\text{O I}]$ line ratio close to 3:1 in the nebular spectra of SN 2017ati indicates optically thin conditions for the emission, but this constraint alone does not provide a direct information on the ejecta geometry. Overall, the $[\text{O I}]$ line profile of SN 2017ati likely reflects a combination of line blending, non-thermal excitation, residual contributions from hydrogen and metal-rich material, and a possible underlying asymmetry in the ejecta, encompassing phenomena similar to those observed in SNe 1993J and 2008ax.

4.4.2. Oxygen mass

The intensity of the $[\text{O I}] \lambda\lambda 6300, 6364$ feature provides an indication of the oxygen mass synthesised in the stellar core, which is closely linked to the progenitor ZAMS mass (Woosley & Weaver 1995; Thielemann et al. 1996). A quantitative determination of the O mass additionally requires the knowledge of the ejecta temperature and the optical depth of the relevant transitions. In this work, the O mass of SN 2017ati is estimated following the method of Jerkstrand et al. (2014), where the O I temperature is inferred from the line ratio of $[\text{O I}] \lambda 5577$ to $[\text{O I}] \lambda\lambda 6300, 6364$, as both lines are collisionally excited and their ratio is sensitive to the temperature.

Measuring the flux of the $[\text{O I}] \lambda\lambda 6300, 6364$ doublet is non-trivial because the red wing is affected by strong and broad emission, likely produced by a blend of $\text{H}\alpha$, He I , and $[\text{N II}]$. As shown in Fig. 9, the observed profile is modelled with four Gaussian components: two account for the $[\text{O I}] \lambda 6300$ and $\lambda 6364$ transitions, while an additional narrow component and a

broad component are introduced to reproduce the blended excess emission (see Sect. 4.4.1). The luminosity of $[\text{O I}]$ is computed through spectral integration, yielding a ratio of $L_{5577}/L_{6300,6364} = 0.33$, with $L_{6300,6364} = 2.7 \times 10^{40} \text{ erg s}^{-1}$. From the same fitting procedure, the flux ratio of $[\text{O I}] \lambda 6300$ to $[\text{O I}] \lambda 6364$ is measured to be 3.2, indicating that the ejecta are already in an optically thin regime at this epoch. Following Jerkstrand et al. (2014), and adopting escape probabilities from Sobolev (1957) and Fransson & Chevalier (1989), we take $\beta_{6300,6364} \approx 0.5$ and $\beta_{5577/6300,6364} \approx 1 - 2$. Using the relation

$$\frac{L_{5577}}{L_{6300,6364}} = 38 \times \exp\left(\frac{-25790 \text{ K}}{T}\right) \beta_{5577/6300,6364}, \quad (3)$$

the oxygen temperature is estimated to lie in the range $T \approx 4740 - 5430$ K. The oxygen mass is then derived from

$$M_{\text{O}} = \frac{L_{6300,6364} / \beta_{6300,6364}}{9.7 \times 10^{41} \text{ erg s}^{-1}} \times \exp\left(\frac{22720 \text{ K}}{T}\right), \quad (4)$$

resulting in an oxygen mass of $M_{\text{O}} \approx 1.82 - 3.34 M_{\odot}$. The inferred oxygen mass exceeds typical values reported for normal SNe II and IIb, including SNe 1993J, 2004et, 2011dh, and 2012aw (Jerkstrand et al. 2012, 2014, 2015a), while being more comparable to those derived for SNe 2015bs and 2018gk (Anderson et al. 2018; Bose et al. 2021).

Stellar evolution models predict a monotonic increase in the oxygen yield with the ZAMS progenitor mass (Nomoto et al. 1997; Rauscher et al. 2002; Limongi & Chieffi 2003; Sukhbold et al. 2016). Within this framework, the measured oxygen mass implies a progenitor initial mass of $M_{\text{ZAMS}} \approx 19 - 26 M_{\odot}$. However, the star rotation can have a significant impact on the oxygen yield (Chieffi & Limongi 2013). For non-rotating progenitors, oxygen masses of 0.50, 1.26, 2.35, and $3.80 M_{\odot}$ correspond to initial masses of 15, 20, 25, and $30 M_{\odot}$, respectively. For rapidly rotating progenitors ($v_{\text{rot}} = 300 \text{ km s}^{-1}$), the yields are substantially higher, reaching 1.48, 2.72, 3.79, and $5.75 M_{\odot}$ for the same masses. Consequently, a rotating progenitor can produce $M_{\text{O}} \approx 1.82 M_{\odot}$ from an initial mass of only $\sim 17 M_{\odot}$, which aligns with the lower-limit progenitor mass estimates discussed later in this paper. Since the oxygen is predominantly synthesised during hydrostatic burning, variations in the explosion physics are expected to have only a limited impact on the relationship between the oxygen mass and the progenitor ZAMS mass. The main sources of uncertainty in the inferred oxygen mass stem from the flux measurements of the $[\text{O I}] \lambda 5577$ and $[\text{O I}] \lambda\lambda 6300, 6364$ lines.

4.4.3. Modeling spectra in the nebular phase

Fransson & Chevalier (1989) proposed that the flux ratio between the $[\text{Ca II}] \lambda\lambda 7291, 7323$ and $[\text{O I}] \lambda\lambda 6300, 6364$ doublets can be used as a semi-quantitative indicator of the ZAMS mass (Fang & Maeda 2018; Fang et al. 2019). This diagnostic is motivated by the different nucleosynthetic origins of the two elements: oxygen is predominantly produced during hydrostatic burning stages, whereas calcium is mainly synthesised during explosive nucleosynthesis. As a consequence, the calcium yield shows only a weak dependence on the prior stellar evolution. A larger $[\text{Ca II}]/[\text{O I}]$ ratio therefore points to a lower initial stellar mass. Furthermore, Elmhamdi et al. (2004) showed that this ratio approaches a stable value at late phases, typically beyond ~ 150 d after the explosion, and remains nearly constant thereafter.

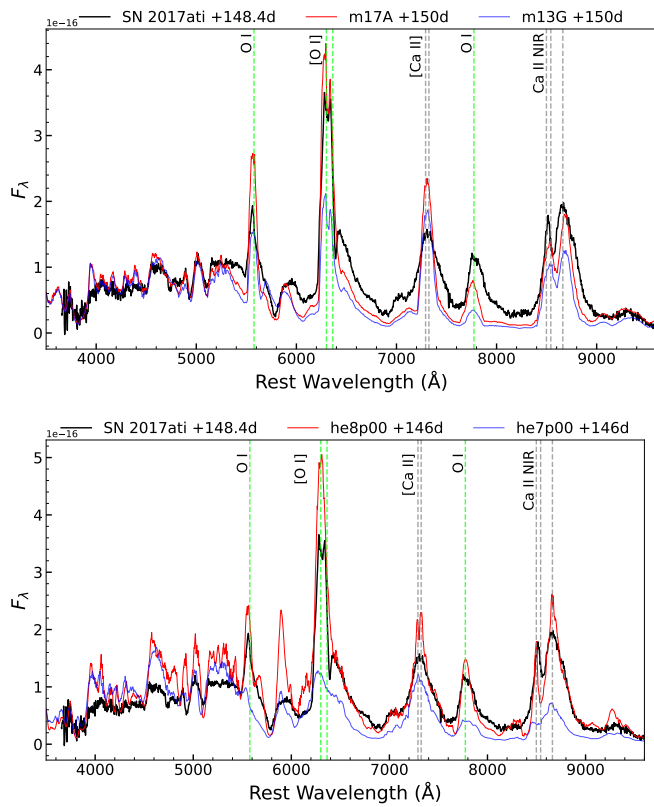


Fig. 10. Nebular-phase spectrum of SN 2017ati at +148.4 d post-explosion (black line), compared with synthetic spectra from different progenitor models. *Upper panel*: Comparison with Type IIb SN models from Jerkstrand et al. (2015a). The blue line represents a model with a progenitor $M_{\text{ZAMS}} = 13 M_{\odot}$, while the red line represents a model with $M_{\text{ZAMS}} = 17 M_{\odot}$. *Lower panel*: Comparison with the he7p00 and he8p00 models presented by Dessart et al. (2023). The blue line denotes the he7p00 model with $M_{\text{preSN}} = 5.04 M_{\odot}$, while the red line corresponds to the he8p00 model with $M_{\text{preSN}} = 5.63 M_{\odot}$. In both panels, the model spectra are scaled to the same distance and the same ^{56}Ni mass as SN 2017ati.

For SN 2017ati, the $[\text{Ca II}]/[\text{O I}]$ flux ratio measured at +148.4 d post-explosion, after the subtraction of the underlying continuum, is approximately 0.50. As discussed in Sect. 4.4.1, this value may be influenced by residual emission from $\text{H}\alpha$, He I , and $[\text{N II}] \lambda\lambda 6548, 6583$, and should therefore be considered as a lower limit. This ratio is comparable to those reported for SN 1993J and SN 2020acat, which are also near 0.5, implying a progenitor ZAMS mass of roughly $14 - 18 M_{\odot}$. However, caution is warranted in interpreting this estimate, as the assumptions underlying the $[\text{Ca II}]/[\text{O I}]$ diagnostic may not be universally applicable to all SNe IIb. For instance, SN 2008ax exhibits a high $[\text{Ca II}]/[\text{O I}]$ ratio despite a relatively massive progenitor (Taubenberger et al. 2011), which is noteworthy given the close similarity in spectral evolution between SN 2017ati and SN 2008ax (see Fig. 8).

The nebular-phase spectrum of SN 2017ati obtained at +148.4 d was compared with synthetic spectra calculated using the SUMO radiative-transfer code (Jerkstrand et al. 2015a), as shown in the upper panel of Fig. 10. The models, computed for an epoch of 150 d, are based on the stellar evolution calculations of Woosley & Heger (2007), considering progenitors with ZAMS mass of $13 M_{\odot}$ (model 13G, originally computed for SN 2008ax and selected here for comparison due to its close

spectral similarity with SNe 2017ati) and $17 M_{\odot}$ (model 17A). For reference, the initial model parameters are summarized as follows: for model 13G, the total ejecta mass is $2.1 M_{\odot}$, the hydrogen envelope mass is $0.054 M_{\odot}$, the helium envelope mass is $1.1 M_{\odot}$, and the initial ^{56}Ni mass is $0.075 M_{\odot}$; for model 17A, the corresponding values are $3.5 M_{\odot}$, $0.054 M_{\odot}$, $1.2 M_{\odot}$, and $0.075 M_{\odot}$, respectively. To ensure a consistent comparison, all model spectra were scaled to the same distance and flux scale as SN 2017ati, adopting a ^{56}Ni mass of $0.21 M_{\odot}$ as inferred in Sect. 3.5 with the radioactive-decay plus magnetar energy-input model. Comparison with nebular spectral models, specifically the 17A model, shows that the $[\text{O I}] \lambda\lambda 6300, 6364$ emission of SN 2017ati is well reproduced, indicating an oxygen mass consistent with a progenitor ZAMS mass of approximately $17 M_{\odot}$. The relative weakness of the $[\text{O I}] \lambda 5577$ line can be explained by a comparatively low nebular temperature or by additional cooling via molecular formation, and does not necessitate a revision of the inferred progenitor mass.

By contrast, the relatively weak $[\text{Ca II}] \lambda\lambda 7291, 7324$ emission, together with the prominent Ca II NIR triplet, reflects physical conditions in the Ca -emitting region rather than a deficiency in calcium mass. Radiative-transfer calculations indicate that the strengths of calcium lines are sensitive to the local density structure, mixing, and the spatial distribution of the radioactive power deposition (Dessart & Hillier 2020). Elevated densities or clumping can suppress the forbidden $[\text{Ca II}]$ transitions while enhancing the permitted Ca II emission. Statistical analyses of nebular spectra presented by Prentice et al. (2022) reveal systematic trends in the $[\text{Ca II}]/[\text{O I}]$ ratio and in the strength of the Ca II NIR emission across different progenitor environments, in agreement with this interpretation (Ergon & Fransson 2022). As discussed in Sect. 4.4.1, the measured fluxes may also be influenced by residual emission from $\text{H}\alpha$, He I , and $[\text{N II}] \lambda\lambda 6548, 6583$, implying that the $[\text{O I}] \lambda\lambda 6300, 6364$ flux could be moderately overestimated.

For Type Ib/Ic SNe arising from completely stripped helium stars, intense stellar winds act to substantially decrease the final pre-SN mass. By contrast, in SNe IIb the survival of a low-mass hydrogen envelope suggests that mass removal from the helium core was relatively modest. This scenario is in line with the conclusions of Dessart et al. (2023), who showed that nebular spectra are primarily governed by the pre-SN mass, with only a weak dependence on the initial stellar mass. We then compare the nebular-phase spectrum of SN 2017ati at +148.4 d with the he7p00 and he8p00 models presented by Dessart et al. (2023), as shown in the lower panel of Fig. 10. The model spectra adopted for this comparison are non-local thermodynamic equilibrium radiative-transfer simulations computed with CMFGEN (Hillier & Dessart 2012), and both models assume a distance of 1 kpc. For the he7p00 model, the adopted parameters are a kinetic energy of $E_{\text{kin}} = 1.38 \times 10^{51} \text{ erg}$, an ejecta mass of $M_{\text{ej}} = 3.33 M_{\odot}$, a ^{56}Ni mass of $M_{\text{Ni}} = 0.102 M_{\odot}$, a pre-explosion mass of $M_{\text{preSN}} = 5.04 M_{\odot}$, and $M_{\text{ZAMS}} = 25.68 M_{\odot}$. The he8p00 model instead adopts $E_{\text{kin}} = 0.71 \times 10^{51} \text{ erg}$, $M_{\text{ej}} = 3.95 M_{\odot}$, $M_{\text{Ni}} = 0.0546 M_{\odot}$, $M_{\text{preSN}} = 5.63 M_{\odot}$, and $M_{\text{ZAMS}} = 27.91 M_{\odot}$. The synthetic spectra from the he7p00 and he8p00 models both show a high degree of similarity to the observed nebular spectrum of SN 2017ati. The most pronounced differences appear in the strengths of the $\text{O I} \lambda\lambda 6300, 6364$ and $\text{Ca II} \lambda\lambda 7291, 7324$ emission features, which are stronger than those predicted by the he7p00 model. In this respect, the he8p00 model provides a closer overall match, reproducing both the relative line strengths and the general spectral morphology more accurately. This level of agreement indicates a progenitor with

a relatively large helium-core mass, consistent with the oxygen mass inferred from the nebular diagnostics and supporting a higher-mass progenitor scenario for SN 2017ati. On this basis, SN 2017ati is more plausibly associated with a pre-SN mass in the range $M_{\text{preSN}} = 5.04 - 5.63 M_{\odot}$. Combining the evidence from the $[\text{Ca II}]/[\text{O I}]$ flux ratio, the $[\text{O I}]$ emission strength, and the comparison with both SUMO and CMFGEN nebular spectral models, we conclude that the progenitor of SN 2017ati likely had a ZAMS mass of $M_{\text{ZAMS}} \geq 17 M_{\odot}$.

5. Discussion

5.1. The nature of light curve evolution

A small group of SNe IIb displaying unusual photometric behaviour has been identified, including SNe 2017ckj, 2018gk, and 2017ati. These objects reach peak luminosities $\approx 1 - 2$ mag brighter in the r band than those of typical SNe IIb (Fig. 1). Their light-curve evolution also differs from that of typical SNe IIb, showing behaviour that is not well matched by either events with a prominent early shock-cooling tail or those without such a feature. If SN 2017ati is assumed to follow a standard SN IIb luminosity evolution powered purely by ^{56}Ni decay, the modelling in Sect. 3.5 using MOSFiT yields a ^{56}Ni mass of $\sim 0.37 M_{\odot}$, while the poor fit to the early-time light curves further indicates that the luminosity is not solely powered by ^{56}Ni . This value is substantially higher than that commonly inferred for normal SNe IIb, for which a mean ^{56}Ni mass of $0.07 \pm 0.03 M_{\odot}$ has been reported in Prentice et al. (2019). Such a high luminosity suggests an additional energy source, such as ejecta-CSM interaction or magnetar spin-down (Bose et al. 2021).

Wang et al. (2017) report that magnetar input dominates the light curve mainly around the maximum light ($t_{\text{exp}} < 50$ d) and again at very late epochs ($t_{\text{exp}} > 300$ d), whereas the decline after peak ($50 \text{ d} < t_{\text{exp}} < 300 \text{ d}$) is largely controlled by the radioactive ^{56}Ni decay. This behaviour closely resembles the light curves for SN 2017ati, which show a relatively high peak luminosity and a rapid decline during the first ~ 50 days after the explosion. Beyond ~ 50 days, the light curves of SN 2017ati exhibit a markedly slower fading, with a decline rate in the Bg bands close to that expected from ^{56}Co radioactive decay ($\sim 0.98 \text{ mag } 100 \text{ d}^{-1}$, see Tab. 1). At very late epochs, however, SN 2017ati lacks sufficient observational coverage, preventing a direct comparison in this phase.

While the magnetar-powered model reduces the inferred nickel mass of SN 2017ati to $M_{^{56}\text{Ni}} = 0.21^{+0.08}_{-0.12} M_{\odot}$, it remains high relative to the typical range of $0.03 - 0.28 M_{\odot}$ reported for SNe IIb (Anderson 2019; Meza & Anderson 2020). This result underscores the exceptional energetics of SN 2017ati compared with more canonical events such as SN 1993J and SN 2011dh, consistent with the relatively high peak luminosity. During the radioactive tail phase, SN 2017ati also remains $\sim 1 - 2$ mag brighter than other SNe IIb.

An alternative explanation for the light curve of SN 2017ati involves additional energy input from ejecta-CSM interaction. Such interaction is classically observed in SNe, which exhibit narrow spectral emission features during the first week after explosion (Fraser 2020). Unfortunately, such early spectroscopic observations are unavailable for SN 2017ati; high-cadence, very early spectroscopy would have been required to break the degeneracy between these two models. Based on the spectra obtained at later phases, a dominant contribution from ejecta-CSM interaction appears unlikely, since such interaction is expected to produce distinctive line-profile morphologies (Dessart & Hillier

2022) or a prominent broad $\text{H}\alpha$ emission similar to that observed in SN 1993J during phases clearly influenced by interaction. Nevertheless, SN 2017ati shows notable spectral similarities to SNe 1993J and 2008ax. In particular, the broad emission feature on the red side of $[\text{O I}] \lambda\lambda 6300, 6364$ may plausibly be associated with $\text{H}\alpha$, as has been suggested for SN 1993J during a transitional phase towards interaction-dominated emission (Matheson et al. 2000). However, the possibility raised by Jerkstrand et al. (2015a), that this feature is instead produced by $[\text{N II}] \lambda\lambda 6548, 6583$ rather than hydrogen, cannot be excluded. By analogy, this makes possible that signatures of ejecta-CSM interaction could emerge at later epochs in SN 2017ati, even if such effects are not prominent in the currently available data.

5.2. Constraints on the progenitor and the explosion

We apply multiple independent methods to constrain the progenitor mass in Sect. 4.4. These methods include nebular-phase spectral diagnostics, based on the luminosities and profiles of oxygen emission lines, together with detailed comparisons to theoretical explosion models. Taken together, these constraints favour a progenitor with a relatively high initial mass ($M_{\text{ZAMS}} \geq 17 M_{\odot}$) and a compact pre-explosion configuration. This interpretation is further supported by the absence of clearly identifiable shock-cooling signatures in the early-time light curves, which argues against a progenitor possessing an extended hydrogen-rich envelope. Moreover, the results of Bamentloo et al. (2024) indicate that helium stars with higher masses are generally associated with smaller stellar radii. While the available evidence points towards a compact progenitor retaining only a low-mass hydrogen-rich envelope, alternative configurations cannot be entirely ruled out given the remaining observational and modelling uncertainties.

Within this framework, different evolutionary channels may in principle give rise to progenitors with similar compact structures. As discussed by Crockett et al. (2008), these channels include a relatively massive single star that lost most of the hydrogen-rich envelope prior to explosion, as well as a lower-mass star that experienced substantial envelope stripping through binary interaction. For SN 2007ati, the nebular-phase $[\text{Ca II}]/[\text{O I}] \sim 0.5$ ratio provides an additional constraint that is sensitive to the progenitor mass (see Sect. 4.4.3), with the observed value being more naturally reproduced by higher-mass progenitor models. The nebular spectra of SN 2017ati show notable similarities to those of SNe 2011fu, 2015as, and 2020acat, characterised by strong $[\text{O I}]$ emission and relatively weak Ca II emission. Given the pronounced spectral similarity of SN 2017ati to SNe 1993J and 2008ax, a progenitor that underwent substantial envelope stripping via binary interaction is favoured, though a massive single-star origin cannot be completely ruled out based on the available observations.

6. Conclusions

SN 2017ati represents an unusual member of the Type IIb SN population. Compared to typical SNe IIb, it exhibits a significantly higher peak luminosity, reaching $M_r = -18.48 \pm 0.16$ mag, approximately 1–2 mag brighter than the typical range. Despite this enhanced peak brightness, the post-peak decline rate beyond ~ 50 d after the explosion is broadly consistent with that of ordinary SNe IIb. The main conclusions of this work are summarised as follows:

- Light-curve modelling of SN 2017ati using `MOSFiT` indicates that a pure ^{56}Ni decay model ($M_{^{56}\text{Ni}} = 0.37^{+0.07}_{-0.10} M_{\odot}$), as well as a ^{56}Ni decay model combined with CSM interaction, fails to adequately reproduce the observed photometric evolution of SN 2017ati. The inclusion of an additional energy contribution from a magnetar yields a notably improved fit, suggesting that such a process may contribute to the luminosity budget.
- The observed light curve of SN 2017ati is better reproduced by a magnetar-powered model ($B = 13.2^{+4.6}_{-4.3} \times 10^{14} \text{ G}$) implemented in `MOSFiT`, compared to alternative models. In this context, the photometric evolution shows similarities to that of SN 1998bw around peak brightness, which have previously been proposed within a magnetar framework. However, the available data do not uniquely distinguish between magnetar input and alternative additional power sources.
- The ^{56}Ni mass, $M_{^{56}\text{Ni}} = 0.21^{+0.08}_{-0.12} M_{\odot}$, inferred from the magnetar-based modelling lies near the upper end of the range typically found for SNe IIb, consistent with the relatively high peak luminosity and the elevated luminosity during the radioactive tail phase of SN 2017ati.
- The optical spectra of SN 2017ati display striking similarities to those of SN 2008ax, with the primary difference being the strength of Ca II emission. This resemblance suggests a comparable explosion configuration and favours a progenitor that experienced substantial envelope stripping through binary interaction, although alternative evolutionary channels cannot be entirely excluded.
- Nebular-phase spectral diagnostics using the luminosities and profiles of oxygen emission lines, combined with comparisons to theoretical explosion models, indicate a ZAMS mass of $M_{\text{ZAMS}} \geq 17 M_{\odot}$ for the progenitor of SN 2017ati.

Upcoming observational facilities, including the Chinese Space Station Telescope (CSST; CSST Collaboration et al. 2025) and the Vera C. Rubin Observatory (Hambleton et al. 2023), will enable time-domain surveys of Type II SNe with substantially improved cadence and sensitivity. Such datasets will enhance the detection and characterisation of rapidly evolving transients, place tighter constraints on theoretical modelling, and contribute to a deeper physical understanding of this complex subclass of CCSNe.

Data availability

Optical photometric measurements of SN 2017ati are available at the CDS via <https://cdsarc.cds.unistra.fr/viz-bin/cat/J/A+A/xxx/xxx>. Our observations of the spectra are available via the Weizmann Interactive SN Data Repository (WISEREP; Yaron & Gal-Yam 2012).

References

Anderson, J. P. 2019, *A&A*, 628, A7
 Anderson, J. P., Dessart, L., Gutiérrez, C. P., et al. 2018, *Nature Astronomy*, 2, 574
 Arcavi, I., Hosseinzadeh, G., Brown, P. J., et al. 2017, *ApJ*, 837, L2
 Arnett, D. C. 1996, in *Supernovae and Nucleosynthesis*
 Arnett, W. D. 1982, *ApJ*, 253, 785
 Balakina, E. A., Pruzhinskaya, M. V., Moskvin, A. S., & Blinnikov, S. I. 2019, in *The Multi-Messenger Astronomy: Gamma-Ray Bursts, Search for Electromagnetic Counterparts to Neutrino Events and Gravitational Waves*, 32–36
 Barbon, R., Benetti, S., Cappellaro, E., et al. 1995, *A&AS*, 110, 513
 Barmentlo, S., Jerkstrand, A., Iwamoto, K., et al. 2024, *MNRAS*, 533, 1251
 Benetti, S. 2017, *Transient Name Server Classification Report*, 2017-258, 1
 Beniamini, P., Hotokezaka, K., van der Horst, A., & Kouveliotou, C. 2019, *MNRAS*, 487, 1426
 Bersten, M. C., Benvenuto, O. G., Nomoto, K., et al. 2012, *ApJ*, 757, 31
 Bersten, M. C., Folatelli, G., García, F., et al. 2018, *Nature*, 554, 497
 Bose, S., Dong, S., Kochanek, C. S., et al. 2021, *MNRAS*, 503, 3472
 Branch, D., Benetti, S., Kasen, D., et al. 2002, *ApJ*, 566, 1005
 Cai, Y. Z., Pastorello, A., Fraser, M., et al. 2018, *MNRAS*, 480, 3424
 Cardelli, J. A., Clayton, G. C., & Mathis, J. S. 1989, *ApJ*, 345, 245
 Charalampopoulos, P., Kotak, R., Sollerman, J., et al. 2025, *A&A*, 700, A138
 Chatzopoulos, E., Wheeler, J. C., Vinko, J., Horvath, Z. L., & Nagy, A. 2013, *ApJ*, 773, 76
 Chevalier, R. A. 1982, *ApJ*, 259, 302
 Chieffi, A. & Limongi, M. 2013, *ApJ*, 764, 21
 Chugai, N. N. 1991, *MNRAS*, 250, 513
 Clocchiatti, A. & Wheeler, J. C. 1997, *ApJ*, 491, 375
 Clocchiatti, A., Wheeler, J. C., Benetti, S., & Frueh, M. 1996, *ApJ*, 459, 547
 Crockett, R. M., Eldridge, J. J., Smartt, S. J., et al. 2008, *MNRAS*, 391, L5
 CSST Collaboration, Gong, Y., Miao, H., et al. 2025, *arXiv e-prints*, arXiv:2507.04618
 Delgado, A., Harrison, D., Hodgkin, S., et al. 2017, *Transient Name Server Discovery Report*, 2017-184, 1
 Desai, D. D., Ashall, C., Shappee, B. J., et al. 2023, *MNRAS*, 524, 767
 Dessart, L. & Hillier, D. J. 2005, *A&A*, 437, 667
 Dessart, L. & Hillier, D. J. 2020, *A&A*, 642, A33
 Dessart, L. & Hillier, D. J. 2022, *A&A*, 660, L9
 Dessart, L., Hillier, D. J., Sukhbold, T., Woosley, S. E., & Janka, H.-T. 2021, *A&A*, 656, A61
 Dessart, L., Hillier, D. J., Woosley, S., et al. 2016, *MNRAS*, 458, 1618
 Dessart, L., Hillier, D. J., Woosley, S. E., & Kuncarayakti, H. 2023, *A&A*, 677, A7
 Dessart, L., Hillier, D. J., Yoon, S.-C., Waldman, R., & Livne, E. 2017, *A&A*, 603, A51
 Elmhamdi, A., Danziger, I. J., Cappellaro, E., et al. 2004, *A&A*, 426, 963
 Ergon, M. & Fransson, C. 2022, *A&A*, 666, A104
 Ergon, M., Sollerman, J., Fraser, M., et al. 2014, *A&A*, 562, A17
 Eyles-Ferris, R. A. J., Jonker, P. G., Levan, A. J., et al. 2025, *ApJ*, 988, L14
 Fang, Q. & Maeda, K. 2018, *ApJ*, 864, 47
 Fang, Q., Maeda, K., Kuncarayakti, H., & Nagao, T. 2024, *Nature Astronomy*, 8, 111
 Fang, Q., Maeda, K., Kuncarayakti, H., Sun, F., & Gal-Yam, A. 2019, *Nature Astronomy*, 3, 434
 Fang, Q., Maeda, K., Kuncarayakti, H., et al. 2022, *ApJ*, 928, 151
 Filippenko, A. V. 1997, *ARA&A*, 35, 309
 Fransson, C. & Chevalier, R. A. 1989, *ApJ*, 343, 323
 Fraser, M. 2020, *Royal Society Open Science*, 7, 200467
 Gal-Yam, A. 2017, in *Handbook of Supernovae*, ed. A. W. Alsabti & P. Murdin, 195
 Gal-Yam, A. 2019, *ARA&A*, 57, 305
 Gangopadhyay, A., Misra, K., Pastorello, A., et al. 2018, *MNRAS*, 476, 3611
 Gangopadhyay, A. & Pessi, P. J. 2025, *arXiv e-prints*, arXiv:2512.04010
 Goldwasser, S., Yaron, O., Sass, A., et al. 2022, *Transient Name Server AstroNote*, 191, 1
 Gomez, S., Berger, E., Nicholl, M., Blanchard, P. K., & Hosseinzadeh, G. 2022, *ApJ*, 941, 107
 González-Gaitán, S., Tominaga, N., Molina, J., et al. 2015, *MNRAS*, 451, 2212
 Grayling, M., Gutiérrez, C. P., Sullivan, M., et al. 2021, *MNRAS*, 505, 3950
 Guillen, J., Nicholl, M., Villar, V. A., et al. 2018, *ApJS*, 236, 6
 Hambleton, K. M., Bianco, F. B., Street, R., et al. 2023, *PASP*, 135, 105002
 Hart, K., Shappee, B. J., Hey, D., et al. 2023, *arXiv e-prints*, arXiv:2304.03791
 Hillier, D. J. & Dessart, L. 2012, *MNRAS*, 424, 252
 Houck, J. C. & Fransson, C. 1996, *ApJ*, 456, 811
 Jerkstrand, A., Ergon, M., Smartt, S. J., et al. 2015a, *A&A*, 573, A12
 Jerkstrand, A., Fransson, C., Maguire, K., et al. 2012, *A&A*, 546, A28
 Jerkstrand, A., Smartt, S. J., Fraser, M., et al. 2014, *MNRAS*, 439, 3694
 Jerkstrand, A., Smartt, S. J., Sollerman, J., et al. 2015b, *MNRAS*, 448, 2482
 Kasen, D. & Bildsten, L. 2010, *ApJ*, 717, 245
 Khatami, D. K. & Kasen, D. N. 2019, *ApJ*, 878, 56
 Kozma, C. & Fransson, C. 1998, *ApJ*, 497, 431
 Kumar, B., Singh, A., Sahu, D. K., & Anupama, G. C. 2022, *ApJ*, 927, 61
 Li, H. & McCray, R. 1992, *ApJ*, 387, 309
 Li, L.-H., Benetti, S., Cai, Y.-Z., et al. 2025a, *A&A*, 704, A233
 Li, W. X., Zhu, Z. P., Zou, X. Z., et al. 2025b, *arXiv e-prints*, arXiv:2504.17034
 Limongi, M. & Chieffi, A. 2003, *ApJ*, 592, 404
 Maeda, K., Tanaka, M., Nomoto, K., et al. 2007, *ApJ*, 666, 1069
 Marinoni, C., Monaco, P., Giuricin, G., & Costantini, B. 1998, *ApJ*, 505, 484
 Matheson, T., Filippenko, A. V., Ho, L. C., Barth, A. J., & Leonard, D. C. 2000, *AJ*, 120, 1499
 Matheson, T., Filippenko, A. V., Li, W., Leonard, D. C., & Shields, J. C. 2001, *AJ*, 121, 1648
 Maurer, J. I., Mazzali, P. A., Deng, J., et al. 2010, *MNRAS*, 402, 161

Mazzali, P. A., Kawabata, K. S., Maeda, K., et al. 2005, *Science*, 308, 1284

Mazzali, P. A., Valenti, S., Della Valle, M., et al. 2008, *Science*, 321, 1185

Medler, K., Mazzali, P. A., Teffs, J., et al. 2022, *MNRAS*, 513, 5540

Meza, N. & Anderson, J. P. 2020, *A&A*, 641, A177

Milisavljevic, D., Fesen, R. A., Gerardy, C. L., Kirshner, R. P., & Challis, P. 2010, *ApJ*, 709, 1343

Modjaz, M., Gutiérrez, C. P., & Arcavi, I. 2019, *Nature Astronomy*, 3, 717

Morales-Garoffolo, A., Elias-Rosa, N., Benetti, S., et al. 2014, *MNRAS*, 445, 1647

Morales-Garoffolo, A., Elias-Rosa, N., Bersten, M., et al. 2015, *MNRAS*, 454, 95

Moriya, T. J., Maeda, K., Taddia, F., et al. 2013, *MNRAS*, 435, 1520

Mould, J. R., Huchra, J. P., Freedman, W. L., et al. 2000, *ApJ*, 529, 786

Nadyozhin, D. K. 1994, *ApJS*, 92, 527

Nagy, A. P. 2018, *ApJ*, 862, 143

Nakar, E. & Piro, A. L. 2014, *ApJ*, 788, 193

Nicholl, M. 2018, *Research Notes of the American Astronomical Society*, 2, 230

Nicholl, M., Guillochon, J., & Berger, E. 2017, *ApJ*, 850, 55

Nomoto, K., Hashimoto, M., Tsujimoto, T., et al. 1997, *Nucl. Phys. A*, 616, 79

Pastorello, A., Kasliwal, M. M., Crockett, R. M., et al. 2008, *MNRAS*, 389, 955

Patat, F., Chugai, N., & Mazzali, P. A. 1995, *A&A*, 299, 715

Peng, Z.-H., Benetti, S., Cai, Y.-Z., et al. 2026, *A&A*, 705, A104

Prentice, S. J., Ashall, C., James, P. A., et al. 2019, *MNRAS*, 485, 1559

Prentice, S. J., Maguire, K., Siebenaler, L., & Jerkstrand, A. 2022, *MNRAS*, 514, 5686

Prentice, S. J., Mazzali, P. A., Pian, E., et al. 2016, *MNRAS*, 458, 2973

Rastinejad, J. C., Levan, A. J., Jonker, P. G., et al. 2025, *ApJ*, 988, L13

Rauscher, T., Heger, A., Hoffman, R. D., & Woosley, S. E. 2002, *ApJ*, 576, 323

Reguitti, A., Pastorello, A., Smartt, S. J., et al. 2025, *A&A*, 698, A129

Richmond, M. W., Treffers, R. R., Filippenko, A. V., & Paik, Y. 1996, *AJ*, 112, 732

Richmond, M. W., Treffers, R. R., Filippenko, A. V., et al. 1994, *AJ*, 107, 1022

Sahu, D. K., Anupama, G. C., & Chakradhari, N. K. 2013, *MNRAS*, 433, 2

Sapir, N. & Waxman, E. 2017, *ApJ*, 838, 130

Schlaflay, E. F. & Finkbeiner, D. P. 2011, *ApJ*, 737, 103

Sharon, A. & Kushnir, D. 2020, *MNRAS*, 496, 4517

Shingles, L., Smith, K. W., Young, D. R., et al. 2021, *Transient Name Server AstroNote*, 7, 1

Sobolev, V. V. 1957, *Soviet Ast.*, 1, 678

Spergel, D. N., Bean, R., Doré, O., et al. 2007, *ApJS*, 170, 377

Srinivasaragavan, G. P., Hamidani, H., Schroeder, G., et al. 2025, *ApJ*, 988, L60

Stritzinger, M. D., Anderson, J. P., Contreras, C., et al. 2018a, *A&A*, 609, A134

Stritzinger, M. D., Taddia, F., Burns, C. R., et al. 2018b, *A&A*, 609, A135

Sukhbold, T., Ertl, T., Woosley, S. E., Brown, J. M., & Janka, H.-T. 2016, *ApJ*, 821, 38

Taddia, F., Stritzinger, M. D., Bersten, M., et al. 2018, *A&A*, 609, A136

Taggart, K. & Perley, D. A. 2021, *MNRAS*, 503, 3931

Tanaka, M., Yamanaka, M., Maeda, K., et al. 2009, *ApJ*, 700, 1680

Taubenberger, S., Navasardyan, H., Maurer, J. I., et al. 2011, *MNRAS*, 413, 2140

Taubenberger, S., Valenti, S., Benetti, S., et al. 2009, *MNRAS*, 397, 677

Thielemann, F.-K., Nomoto, K., & Hashimoto, M.-A. 1996, *ApJ*, 460, 408

Thomas, R. C. 2013, *SYN++: Standalone SN spectrum synthesis*, *Astrophysics Source Code Library*, record ascl:1308.008

Thomas, R. C., Nugent, P. E., & Meza, J. C. 2011, *PASP*, 123, 237

Tsvetkov, D. Y., Volkov, I. M., Baklanov, P., Blinnikov, S., & Tuchin, O. 2009, *Peremennye Zvezdy*, 29, 2

Tsvetkov, D. Y., Volkov, I. M., Sorokina, E., et al. 2012, *Peremennye Zvezdy*, 32, 6

Valenti, S., Fraser, M., Benetti, S., et al. 2011, *MNRAS*, 416, 3138

Wang, L. J., Yu, H., Liu, L. D., et al. 2017, *ApJ*, 837, 128

Wang, Z. Y., Pastorello, A., Maeda, K., et al. 2024, *A&A*, 691, A156

Woosley, S. E. 2010, *ApJ*, 719, L204

Woosley, S. E. & Heger, A. 2007, *Phys. Rep.*, 442, 269

Woosley, S. E. & Weaver, T. A. 1995, *ApJS*, 101, 181

Yaron, O. & Gal-Yam, A. 2012, *PASP*, 124, 668

Young, D. R. 2020, *plot_atlas_fp.py*

Zhao, J.-W., Benetti, S., Cai, Y.-Z., et al. 2025, *arXiv e-prints*, arXiv:2512.09384

Zhu, J.-P., Zheng, J.-H., & Zhang, B. 2025, *MNRAS*, 544, L139

¹ School of Electronic Science and Engineering, Chongqing University of Posts and Telecommunications, Chongqing 400065, P.R. China

² INAF - Osservatorio Astronomico di Padova, Vicoletto dell'Osservatorio 5, 35122 Padova, Italy

³ Yunnan Observatories, Chinese Academy of Sciences, Kunming 650216, P.R. China

⁴ International Centre of Supernovae, Yunnan Key Laboratory, Kunming 650216, P.R. China

⁵ South-Western Institute for Astronomy Research, Yunnan Key Laboratory of Survey Science, Yunnan University, Kunming, Yunnan 650500, P.R. China

⁶ Yunnan Key Laboratory of Survey Science, Yunnan University, Kunming, Yunnan 650500, P.R. China

⁷ INAF - Osservatorio Astronomico di Brera, Via E. Bianchi 46, 23807 Merate (LC), Italy

⁸ School of Astronomy and Space Science, University of Chinese Academy of Sciences, Beijing 100049, P.R. China

⁹ National Astronomical Observatories, Chinese Academy of Sciences, Beijing 100101, P.R. China

¹⁰ Institute of Space Sciences (ICE, CSIC), Campus UAB, Carrer de Can Magrans, s/n, E-08193 Barcelona, Spain

¹¹ National Astronomical Observatory of Japan, National Institutes of Natural Sciences, 2-21-1 Osawa, Mitaka, Tokyo 181-8588, Japan

¹² School of Physics, O'Brien Centre for Science North, University College Dublin, Belfield, Dublin 4, Ireland

¹³ innish Centre for Astronomy with ESO (FINCA), FI-20014 University of Turku, Finland

¹⁴ Department of Physics and Astronomy, University of Turku, FI-20014 Turku, Finland

¹⁵ Kapteyn Astronomical Institute, University of Groningen, 9700 AV Groningen, The Netherlands

¹⁶ The Oskar Klein Centre, Department of Astronomy, Stockholm University, AlbaNova, SE-10691 Stockholm, Sweden

¹⁷ School of Sciences, European University Cyprus, Diogenes Street, Engomi, 1516 Nicosia, Cyprus

¹⁸ Cosmic Dawn Center (DAWN)

¹⁹ Niels Bohr Institute, University of Copenhagen, Jagtvej 128, DK-2200, Copenhagen N, Denmark

²⁰ Department of Physics and Astronomy, Aarhus University, Ny Munkegade 120, DK-8000 Aarhus C, Denmark

²¹ School of Physics and Electrical Engineering, Liupanshui Normal University, Liupanshui, Guizhou, 553004, P.R. China

²² Department of Mathematics and Physics, School of Biomedical Engineering, Southern Medical University, Guangzhou 510515, P.R. China

Appendix A: Acknowledgements

We thank Luc Dessart for his invaluable contributions to the interpretation of light curves and spectra, as well as his insightful comments and revisions that significantly improved this work. This work is supported by the National Natural Science Foundation of China (No. 12303054), the National Key Research and Development Program of China (Grant No. 2024YFA1611603), the Yunnan Fundamental Research Projects (Grant Nos. 202401AU070063, 202501AS070078), and the International Centre of Supernovae, Yunnan Key Laboratory (No. 202302AN360001). AP, AR, SB, EC, NER and LT acknowledge support from the PRIN-INAF 2022, "Shedding light on the nature of gap transients: from the observations to the models". AR also acknowledges financial support from the GRAWITA Large Program Grant (PI P. D'Avanzo). EC acknowledges support from MIUR, PRIN 2020 (METE, grant 2020KB33TP). N.E.R. also acknowledges support from the Spanish Ministerio de Ciencia e Innovación (MCIN) and the Agencia Estatal de Investigación (AEI) 10.13039/501100011033 under the program Unidad de Excelencia María de Maeztu CEX2020-001058-M. T.K. acknowledges support from the Research Council of Finland project 360274. T.M.R is part of the Cosmic Dawn Center (DAWN), which is funded by the Danish National Research Foundation under grant DNRF140. T.M.R and S. Mattila acknowledge support from the Research Council of Finland project 350458. M.D.S. is funded by the Independent Research Fund Denmark (IRFD, grant number 10.46540/2032-00022B). S.-P. Pei is supported by the Science and Technology Foundation of Guizhou Province (QKHJC-ZK[2023]442). Y.-J. Yang is supported by the National Natural Science Foundation of China (Grants No. 12305066). We thank Luhan Li for providing some public datasets of comparison objects.

Based on observations obtained with the Cima Ekar 1.82 m Telescopio Copernico, installed at the INAF (Istituto Nazionale di Astrofisica) - Astronomical Observatory of Padova, Italy. Based on observations made with the Nordic Optical Telescope (NOT), owned in collaboration by the University of Turku and Aarhus University, and operated jointly by Aarhus University, the University of Turku, and the University of Oslo, representing Denmark, Finland, and Norway, the University of Iceland, and Stockholm University at the Observatorio del Roque de los Muchachos, La Palma, Spain, of the Instituto de Astrofisica de Canarias.

We acknowledge ESA Gaia, DPAC and the Photometric Science Alerts Team (<http://gsaweb.ast.cam.ac.uk/alerts>). This work has made use of data from the Asteroid Terrestrial-impact Last Alert System (ATLAS) project. ATLAS is primarily funded to search for near-Earth objects through NASA grants NN12AR55G, 80NSSC18K0284, and 80NSSC18K1575; byproducts of the NEO search include images and catalogs from the survey area. The ATLAS science products have been made possible through the contributions of the University of Hawaii Institute for Astronomy, the Queen's University Belfast, STScI, and the South African Astronomical Observatory, and The Millennium Institute of Astrophysics (MAS), Chile. We thank Las Cumbres Observatory and its staff for their continued support of ASAS-SN. ASAS-SN is funded in part by the Gordon and Betty Moore Foundation through grants GBMF5490 and GBMF10501 to the Ohio State University, and also funded in part by the Alfred P. Sloan Foundation grant G-2021-14192. Development of ASAS-SN has been supported by NSF grant AST-0908816, the Mt. Cuba Astronomical Foundation, the Center for Cosmology and AstroParticle Physics at the Ohio State University, the Chinese Academy of Sciences South America Center for Astronomy (CAS-SACA), and the Villum Foundation. This research has made use of the NASA/IPAC Extragalactic Database (NED), which is operated by the Jet Propulsion Laboratory, California Institute of Technology, under contract with the National Aeronautics and Space Administration. IRAF was distributed by the National Optical Astronomy Observatory, which was managed by the Association of Universities for Research in Astronomy (AURA), Inc., under a cooperative agreement with the U.S. NSF.

Appendix B: Observations and data reductions

B.1. Photometric data

We performed optical photometric follow-up of SN 2017ati in multiple bands, covering the Sloan *ugriz* and Johnson–Bessell *BV* systems, starting shortly after its discovery. The observations were conducted using several ground-based facilities. The 1.82 m Copernico Telescope, fitted with the Asiago Faint Object Spectrograph and Camera (AFOSC), is operated by the INAF Padova Astronomical Observatory at the Asiago Observatory in Italy. The 2.56 m Nordic Optical Telescope (NOT) was employed with the Alhambra Faint Object Spectrograph and Camera (ALFOSC).

The optical photometry from the ground-based facilities was reduced using the *ecsnoopy*¹⁰ pipeline, adopting the data-processing methodology outlined by Cai et al. (2018). In addition to our own observations, we collected publicly available archival photometric data from several surveys, including the Asteroid Terrestrial-impact Last Alert System (ATLAS), *Gaia*¹¹, and the All-Sky Automated Survey for Supernovae (ASAS-SN). The ATLAS orange (*o*)- and cyan (*c*)-band light curves were extracted using the ATLAS Forced Photometry service¹² (Shingles et al. 2021).

The ATLAS photometric measurements were further processed using a script described by Young (2020), which applies a rolling-window algorithm to identify and remove spurious points and bins the remaining data into 1-d intervals. Additional *V*-band photometry was retrieved from the ASAS-SN Sky Patrol¹³ (Hart et al. 2023). The final calibrated optical photometry of SN 2017ati has been made publicly available through the Strasbourg Astronomical Data Centre (CDS).

B.2. Spectroscopic data

Spectroscopic follow-up observations of SN 2017ati were obtained with the 1.82m Copernico Telescope equipped with AFOSC and the 2.56m NOT using ALFOSC. The spectra acquired with both Copernico/AFOSC and NOT/ALFOSC were reduced with the dedicated FoscGUI¹⁴ pipeline.

All raw spectroscopic frames were reduced following standard procedures using *IRAF*. The basic reduction steps included bias subtraction, overscan correction, flat-field correction, and image trimming, consistent with those applied to the imaging data. One-dimensional spectra were then extracted from the two-dimensional frames. Wavelength calibration was performed using arc-lamp exposures obtained during the same observing nights, while flux calibration relied on observations of spectrophotometric standard stars. Telluric absorption features, primarily due to O₂ and H₂O, were corrected using the standard-star spectra. The reliability of the flux calibration was verified by comparing synthetic photometry derived from the spectra with contemporaneous broadband photometric measurements. A summary of the instruments and observational setups employed for the spectroscopic data is provided in Table C.1 in Appendix C.

Appendix C: Supplementary tables

¹⁰ *ecsnoopy* is a software for SN photometry employing PSF fitting and/or template subtraction, developed by E. Cappellaro. Documentation is available at <https://sngroup.oapd.inaf.it/ecsnoopy.html>.

¹¹ <http://gsaweb.ast.cam.ac.uk/alerts>

¹² <https://fallingstar-data.com/forcedphot/>

¹³ <https://asas-sn.osu.edu>

¹⁴ FoscGUI is a graphic user interface aimed at extracting SN spectroscopy and photometry obtained with FOSC-like instruments. It was developed by E. Cappellaro. A package description can be found at <http://sngroup.oapd.inaf.it/foscgui.html>.

Table C.1. Log of spectroscopic observations of SN 2017ati.

Date	MJD	Phase ^a [days]	Telescope+Instrument	Grism/Grating+Slit	Spectral range [Å]	Resolution [Å]	Exp.time [s]
2017-02-27	57811.8	+27.3	Copernico 1.82m+AFOSC	GR04+1.69"	3430 – 8110	13.7	1800
2017-03-09	57826.0	+41.5	NOT+ALFOSC	gm4+1.3"	3300 – 8860	17.7	1800
2017-03-17	57829.8	+45.3	Copernico 1.82m+AFOSC	VPH7+1.69"	3600 – 9150	14.6	1800
2017-03-25	57837.0	+52.5	Copernico 1.82m+AFOSC	VPH6+1.69"	3670 – 9150	14.4	1800
2017-03-28	57840.0	+55.5	Copernico 1.82m+AFOSC	VPH7+1.69"	3600 – 9140	15.1	2400
2017-04-06	57849.1	+64.6	NOT+ALFOSC	gm4+1.3"	3560 – 9500	17.7	1800
2017-04-21	57864.9	+80.4	NOT+ALFOSC	gm4+1.0"	3650 – 9400	13.7	1250
2017-05-08	57881.9	+97.4	NOT+ALFOSC	gm4+1.3"	3800 – 9500	17.9	1800
2017-05-30	57903.9	+119.4	NOT+ALFOSC	gm4+1.0"	3660 – 9540	13.9	1800
2017-06-28	57932.9	+148.4	NOT+ALFOSC	gm4+1.0"	3640 – 9540	14.0	3200

^a Phases are calculated relative to the explosion epoch (MJD = 57784.5) in the reference frame of the observer.

Table C.2. Parameters for the comparison sample of SNe IIb.

SN IIb	Explosion Date [MJD]	Redshift <i>z</i>	Distance [Mpc]	$E(B-V)_{\text{Gal}}$ [mag]	$E(B-V)_{\text{Host}}$ [mag]	$M_{r/R}^{\text{peak}}{}^a$ [mag]	$L_{\text{peak}}{}^a$ [erg s ⁻¹]	References
1993J	49072.0	-0.000113	2.9	0.069	0.11	-17.73 ± 0.33	1.43×10^{42}	1
2008ax	54528.8	0.00456	9.6 ± 1.3	0.022	0.278	-17.28 ± 0.46	1.30×10^{42}	2
2011dh	55712.5	0.001638	8.03 ± 0.77	0.03	0.04	-17.50 ± 0.22	8.93×10^{41}	3
2011fu	55824.5	0.001845	74.5 ± 5.2	0.068	0.035	-17.89 ± 0.12	1.89×10^{42}	4
2013df	56449.5	0.00239	21.38 ± 2.95	0.017	0.081	-17.00 ± 0.08	7.51×10^{41}	5
2015as	57332.0	0.0036	19.2 ± 1.4	0.008	0	~ -17.28	8.49×10^{41}	6
2016gkg	57651.2	0.0049	21.8	0.0166	0.09	~ -17.53	1.05×10^{42}	7
2017ckj	57836.6	0.037	158.1 ± 11.1	0.013	0	-18.46 ± 0.07	6.59×10^{42}	8
2018gk	58130.1	0.031010	140.5 ± 2.3	0.0086	0	-19.64 ± 0.24	1.43×10^{43}	9
2020acat	59192.0	0.007932	35.3 ± 4.4	0.0207	0	-16.55 ± 0.35	1.48×10^{42}	10
2021bxu	59246.3	0.0178	72±5	0.014	0	~ 15.93	3.79×10^{41}	11
2022ngb	59749.9	0.00965	32.2 ± 2.8	0.085	0.085	-16.55 ± 0.35	7.85×10^{41}	12
2024abfo	60628.3	0.003512	10.85 ± 0.53	0.0097	0	-16.50 ± 0.10	7.23×10^{41}	13
2017ati	57784.5	0.01696	70.80 ± 5.20	0.104	0	-18.48 ± 0.16	3.00×10^{42}	14

^a Peak magnitudes and luminosities refer to the maximum.

References: 1= Richmond et al. (1994), Barbon et al. (1995), Richmond et al. (1996), 2= Pastorello et al. (2008), Tsvetkov et al. (2009), Taubenberger et al. (2011), 3= Tsvetkov et al. (2012), Sahu et al. (2013), Ergon et al. (2014), 4= Morales-Garoffolo et al. (2015), 5=Morales-Garoffolo et al. (2014), 6=Gangopadhyay et al. (2018), 7= Arcavi et al. (2017), Bersten et al. (2018), 8=Li et al. (2025a), 9= Bose et al. (2021), 10= Medler et al. (2022), 11= Desai et al. (2023), 12=Zhao et al. (2025) , 13=Reguitti et al. (2025), 14=This Work.

Table C.3. Estimated ^{56}Ni mass from different methods.

Method	$M_{\text{Ni}} (M_{\odot})$
Arnett, peak, pseudo-bol	0.40 ± 0.09
Clocchiatti & Wheeler (1997), peak, pseudo-bol	$0.29^{+0.05}_{-0.04}$
1987A, tail, pseudo-bol	0.47 ± 0.13
MOSFiT, Pure ^{56}Ni	$0.37^{+0.07}_{-0.10}$
MOSFiT, ^{56}Ni + CSM	$0.74^{+0.20}_{-0.15}$
MOSFiT, ^{56}Ni + Magnetar	$0.21^{+0.08}_{-0.12}$

Table C.4. Marginalised posteriors for the MOSFiT model of SN 2017ati.

Parameter	^{56}Ni	$^{56}\text{Ni} + \text{CSM}$	$^{56}\text{Ni} + \text{Magnetar}$	Units
B	–	–	$13.18^{+4.60}_{-4.27}$	$10^{14} G$
P_{spin}	–	–	$28.18^{+3.72}_{-6.3}$	ms
$n_{\text{H,host}}$	–	$28.18^{+2.72}_{-2.48}$	–	10^{20} cm^{-2}
E_{k}	–	$1.10^{+0.16}_{-0.07}$	–	10^{51} erg
M_{CSM}	–	$1.23^{+0.25}_{-0.13}$	–	M_{\odot}
R_0	–	$29.51^{+24.19}_{-11.32}$	–	AU
ρ_0	–	$6.67^{+11.34}_{-4.13}$	–	$10^{-13} \text{ g cm}^{-3}$
M_{ej}	$1.70^{+0.44}_{-0.38}$	$4.90^{+0.72}_{-0.53}$	$1.82^{+0.53}_{-0.59}$	M_{\odot}
$M_{^{56}\text{Ni}}$	$0.37^{+0.07}_{-0.10}$	$0.74^{+0.20}_{-0.15}$	$0.21^{+0.08}_{-0.12}$	M_{\odot}
κ_y	$0.06^{+0.03}_{-0.01}$	$0.06^{+0.02}_{-0.01}$	$0.33^{+0.12}_{-0.05}$	$\text{cm}^2 \text{ g}^{-1}$
T_{min}	$4.47^{+0.21}_{-0.20}$	$6.61^{+0.31}_{-0.30}$	$4.57^{+0.11}_{-0.10}$	10^3 K
σ	$0.37^{+0.03}_{-0.02}$	$0.20^{+0.01}_{-0.01}$	$0.17^{+0.01}_{-0.02}$	–
v_{ej}	$3.63^{+0.26}_{-0.24}$	$6.12^{+0.83}_{-0.60}$	$7.24^{+0.70}_{-0.64}$	10^3 km s^{-1}
t_{exp}	$-33.97^{+4.55}_{-1.03}$	-5.0	$-7.36^{+0.64}_{-0.99}$	days

Appendix D: Supplementary figures

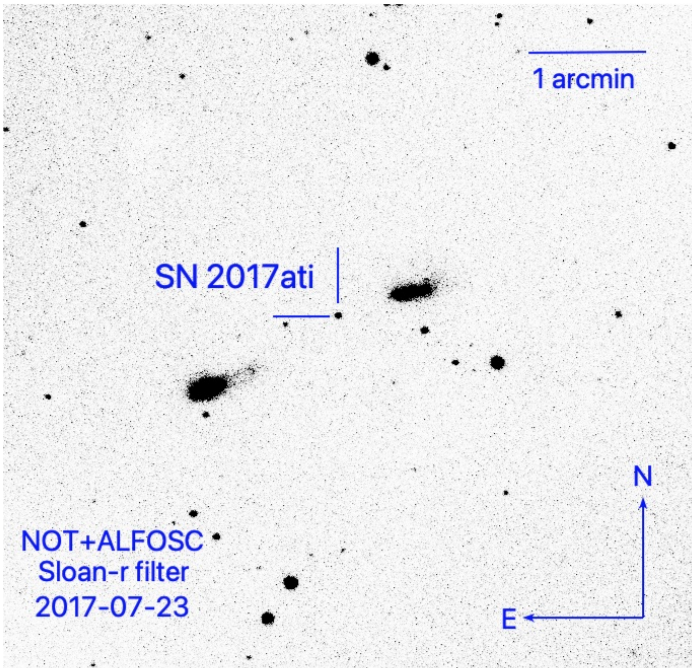


Fig. D.1. An image showing the location of SN 2017ati, obtained on July 23, 2017, using the r -Sloan filter with the NOT/ALFOSC. The orientation and scale are included.

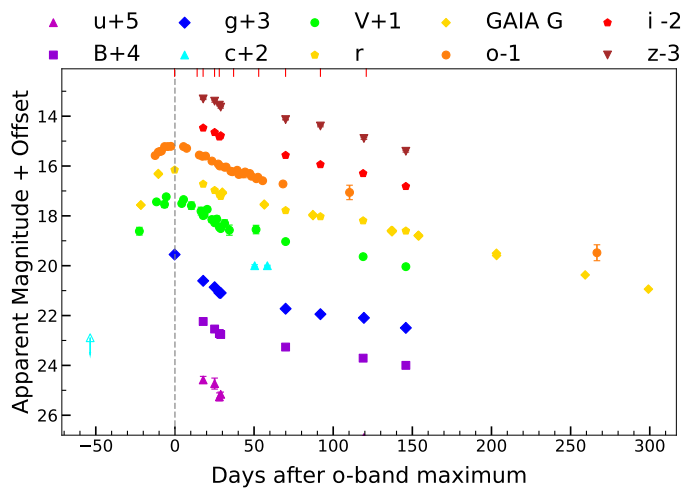


Fig. D.2. Multi-band light curves of SN 2017ati. The dashed vertical line marks the reference epoch, corresponding to the maximum light in the o band. Epochs of our spectroscopic observations are indicated by solid red vertical lines at the top. Upper limits are represented by empty symbols with downward arrows. For clarity, the light curves have been vertically offset by constant values, as indicated in the legend. In most cases, the magnitude uncertainties are smaller than the sizes of the plotted symbols.

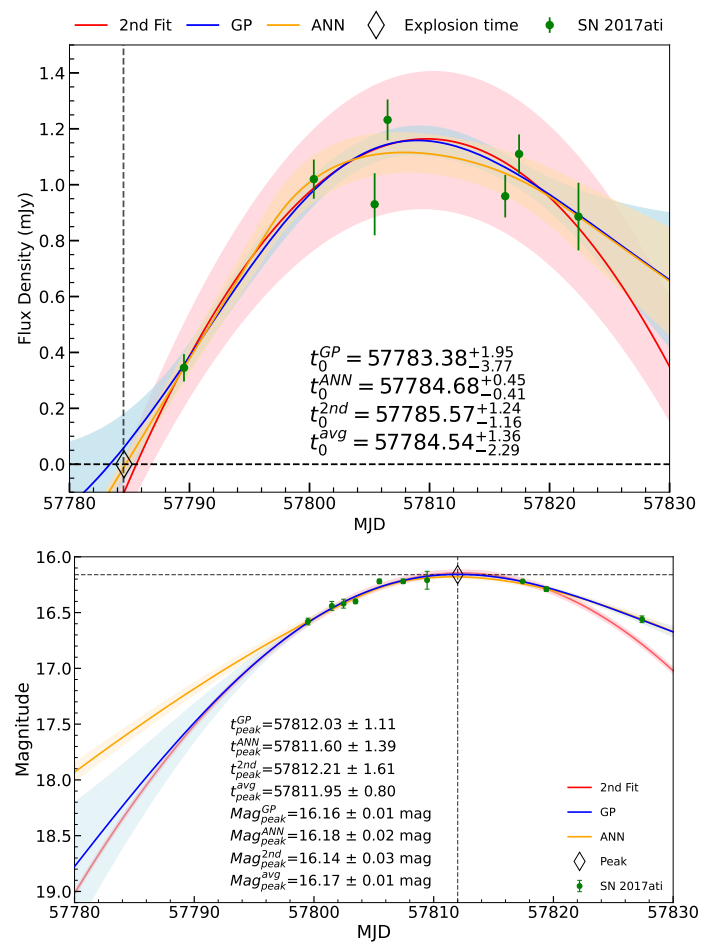


Fig. D.3. The fitted explosion and peak epochs of SN 2017ati are shown. *Upper panel:* the ASAS-SN V -band light curve in flux space (mJy) is fitted with a solid line, and the shaded region represents the 3σ uncertainty of the explosion epoch. *Lower panel:* the o -band light curve is fitted with a solid line, with the shaded region indicating the 3σ uncertainty of the peak epoch.

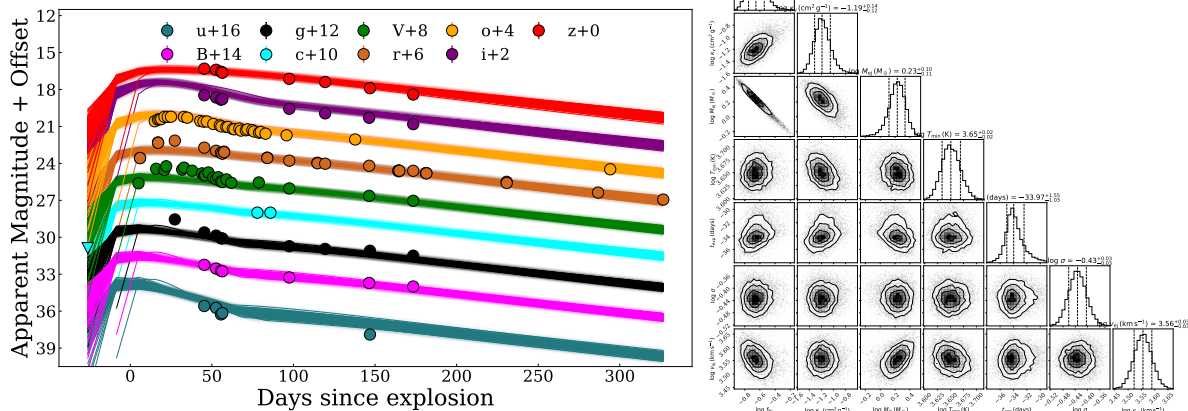


Fig. D.4. Multi-band light curve of SN 2017ati fitted with the radioactive decay model by MOSFiT, together with the parameter posteriors from the MCMC sampling displayed in the corner plot. The relevant parameters are listed in Table C.4.

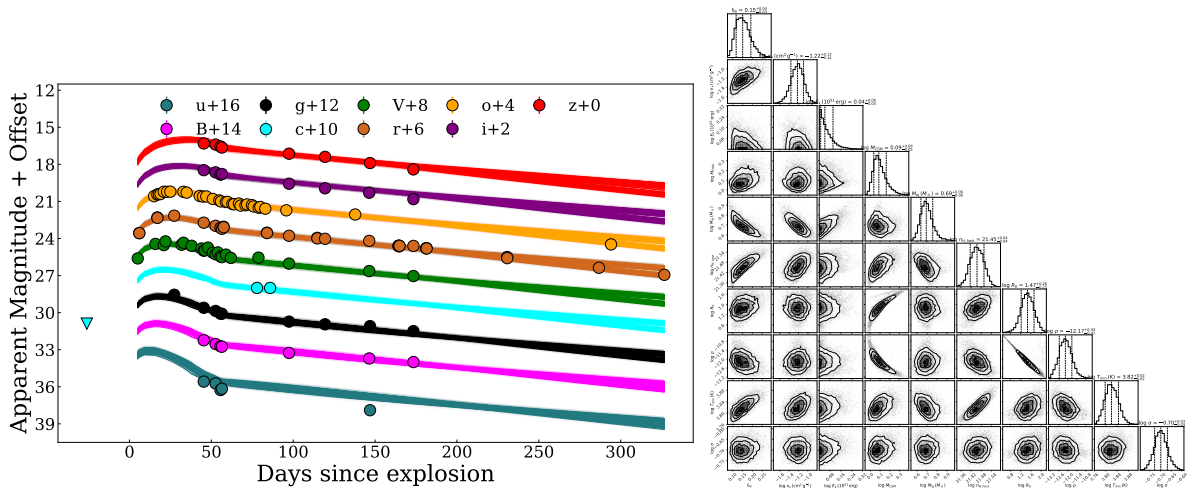


Fig. D.5. Multi-band light curve of SN 2017ati reproduced with the combined radioactive decay and CSM interaction model in MOSFiT, with the corner plot showing constraints from the MCMC sampling. The relevant parameters are listed in Table C.4.

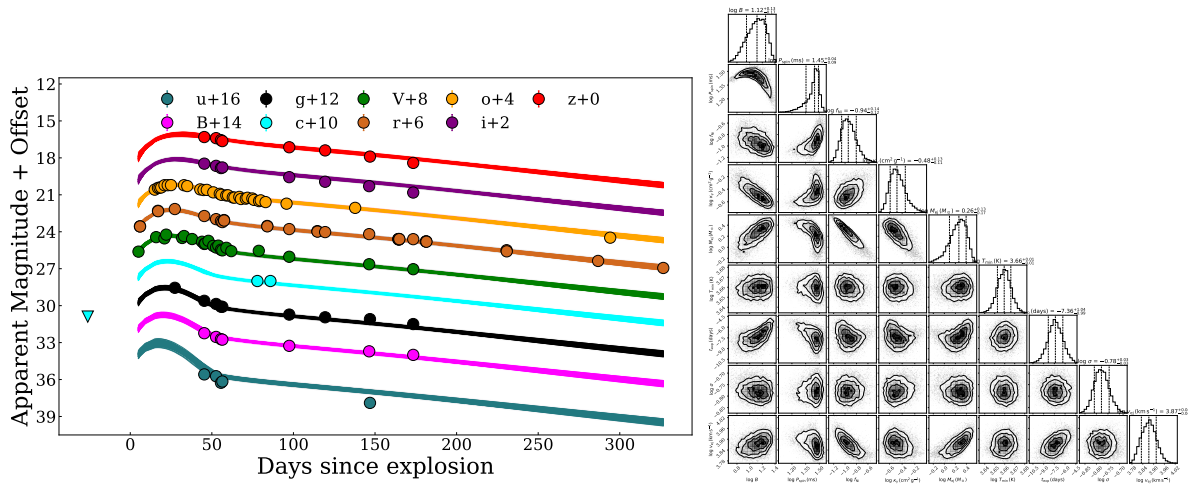


Fig. D.6. Multi-band light curve of SN 2017ati reproduced with the radioactive decay plus magnetar central-engine model in MOSFiT, with the corner plot showing constraints from the MCMC sampling. The relevant parameters are listed in Table C.4.